Future Circular Collider

PUBLICATION

Preliminary EIR design including optimized lattice deck: Deliverable D3.3

Tomas Garcia, Rogelio (CERN) *et al.*

30 January 2019

The research leading to this document is part of the Future Circular Collider Study

The electronic version of this FCC Publication is available on the CERN Document Server at the following URL :
<http://cds.cern.ch/record/2655283>

Grant Agreement No. 654305

EuroCirCol

European Circular Energy-Frontier Collider Study

Horizon 2020 Research and Innovation Framework Programme, Research and Innovation Action

DELIVERABLE REPORT

PRELIMINARY EIR DESIGN INCLUDING OPTIMIZED LATTICE DECK

Document identifier:	EuroCirCol-P3-WP3-D3.3
Due date:	End of month 44 (February 1, 2019)
Report release date:	30/01/2019
Work package:	WP3 (Experimental Interaction Region)
Lead beneficiary:	CERN
Document status:	RELEASED (V1.0)

Abstract:

Annotated beam optics and lattice files with specifications of the required magnet parameters (strengths and apertures) including consolidated position and element characteristics. Specification of the required magnet types and quantities including magnet field quality specifications.

Delivery Slip

	Name	Partner	Date
Authored by	Jose Abelleira Emilia Cruz-Alaniz Léon Van Riesen-Haupt Andrei Seryi Sergey Arsenyev Michael Benedikt Maria Ilaria Besana Xavier Buffat Helmut Burkhardt Francesco Cerutti Michael Hofer Barbara L. Humann Angelo Infantino Jacqueline Keintzel Andy Langner Roman Martin Werner Riegler Daniel Schulte Rogelio Tomás Frank Zimmermann Robert B. Appleby Haroon Rafique Javier Barranco Tatiana Pieloni Claudia Tambasco Manuela Boscolo Francesco Collamati Oscar Blanco García David Boutin Antoine Chancé Barbara Dalena	UOXF CERN STFC EPFL INFN CEA	17/01/2019
Edited by	Julie Hadre Johannes Gutleber	CERN	17/01/2019
Reviewed by	Michael Benedikt Daniel Schulte	CERN	23/01/2019
Approved by	EuroCirCol Coordination Committee		30/01/2019

TABLE OF CONTENTS

1 OVERVIEW

FCC-hh will provide proton-proton collisions at a center-of-mass energy of 100 TeV, a factor 7 higher that the LHC. The goal for the integrated luminosity is set to $20 \, ab^{-1}$ in each high luminosity experiment. This ambitious goal can be reached by an operational scenario with 10 years of operation using the less ambitious parameters (Baseline option) followed by 15 years of operation at ultimate parameters. Table 1 shows the two parameter sets for the high luminosity IRs and compares them with the respective parameters of LHC and HL-LHC. The most notable difference between Baseline and Ultimate are the goals for the β functions at the interaction point, β^*, leading to a significant increase in instantaneous luminosity at ultimate optics. Due to the high center-of-mass energy and the high luminosity the total power released at the IP towards each side increases from 1 kW in the LHC or 4.75 kW in HL-LHC up to 260 kW in FCC-hh at ultimate parameters. Most of this power will be absorbed in the detector but debris particles emitted at small angles will travel down the beam pipe and impact in the interaction region magnets, possibly causing quenches and degrading the material. Consequently, the radiation load from collision debris has been identified as a key issue of the final focus system early in the design phase of the interaction regions [1]. Unifying adequate protection of the triplet magnets with a high luminosity performance has been the driving factor of the interaction region layout.

In terms of the chromaticity correction it has been estimated that the sextupoles in the arcs are able to correct around 557 units of chromaticity. The natural chromaticity for the case with β^*=30 cm is below this value, and therefore the chromaticity can be corrected. However this is not the case for beyond ultimate optics. While the aperture of the final focus system can accommodate a β^* of almost 20 cm, the strength of the sextupoles necessary to correct the chromaticity is above the achievable maximum.

Although the high mass of protons usually keeps the synchrotron radiation produced in hadron colliders low, the high beam energy of FCC-hh gives rise to the concern that the photon background in the experimental regions might grow to notable levels. Hence, a closer investigation synchrotron radiation was necessary in order to quantify the impact. The simulation of the photon background concluded that the synchrotron radiation is not expected to be an issue for the experiments.

Debris from proton collision at the interactions points may create background in the other detectors. Protons with an energy close to the nominal beam energy traveling far in the beam pipe before being intercepted, as well as muons passing through the rock between two experiments are of particular concern. Tracking studies of the protons and an analysis of the muon range in rock were performed, concluding that the cross talk between experiments is negligible.

The high luminosity EIR design relies on the availability of crab cavities to compensate the luminosity loss due to the crossing angle. As this technology is currently being tested in proton accelerators for the first time it is desirable to have an alternative that avoids crab cavities. Flat beam optics are a good candidate for this as the crossing angle in the less squeezed plane can be kept rather small, reducing the luminosity loss from the geometric overlap of the colliding bunches. Corresponding optics have been developed, using an alternative triplet layout.

In addition to the two high luminosity interaction regions (IRs) situated in the Points A and G, FCC-hh features two low luminosity interaction regions in the points B and L, much like the LHC. In absence of a physics case – and consequently luminosity goals or space constraints – for these two experimental regions, an initial design is proposed that can reach an integrated

Table 1: *Key parameters of FCC-hh compared to LHC and HL-LHC. Note that parameters in paranthesis in the FCC-hh column relate to the option with 5 ns bunch spacing.*

	LHC	HL-LHC	FCC-hh Baseline	Ultimate
Center-of-mass energy [TeV]	14	14	100	
Injection energy [TeV]	0.45	0.45	3.3	
Ring circumference [km]	26.7	26.7	97.75	
Arc dipole field [T]	8.33	8.33	16	
Number of IPs	2+2	2+2	2+2	
Number of bunches per beam n_b	2808	2748	10600 (53000)	
Beam current [A]	0.58	1.11	0.5	
Peak luminosity/IP [10^{34} cm^{-2}s^{-1}]	1	5	5	30
Events/crossing	27	135	170	1020 (204)
Stored beam energy [GJ]	0.4	0.7	8.4	
Synchrotron power per beam [MW]	0.0036	0.0073	2.4	
Arc synchrotron radiation [W/m/beam]	0.18	0.35	28.4	
IP beta function β^* [m]	0.4	0.15	1.1	0.3
Bunch spacing [ns]	25	25	25 (5)	
Initial norm. rms emittance [µm]	3.75	2.5	2.2 (0.45)	
Initial bunch population N_b[10^{11}]	1.15	2.2	1.0 (0.2)	
Transv. emittance damping time [h]	25.8	25.8	1.1	
RMS bunch length [cm]	7.55		8	
RMS IP beam size [µm]	16.7	7.1	6.8	3.5 (1.6)
Full crossing angle [µrad]	285	590	104	200

luminosity of $500 \, \text{fb}^{-1}$. An alternative for the low luminosity IRs is FCC-eh [2, Sec. 2.8], a lepton-hadron collider with interaction region scaled up from the LHeC [3].

A filling scheme with 5 ns bunch spacing is considered to mitigate the event pile-up in the detectors. The corresponding parameters are shown in Table 1 in parenthesis. This option has not been addressed in the IR design although it reduces aperture needs thanks to the lower emittance and could pose operational difficulties to keep beams in collision as the beam size reduces below 1 μm during the physics fill due to synchrotron radiation damping.

Simulations of collective effects revealed that the beams could become unstable while bringing them into collision at $\beta^* = 0.3$ m due to the loss of Landau damping. An easy mitigation without a significant penalty in integrated luminosity would be to collide beams at larger β^* and continue the β^* squeeze while colliding. This is usually referred to as collide & squeeze. Figure 1 shows an illustration of how FCC-hh physics fill would look like with and without resorting to collide & squeeze.
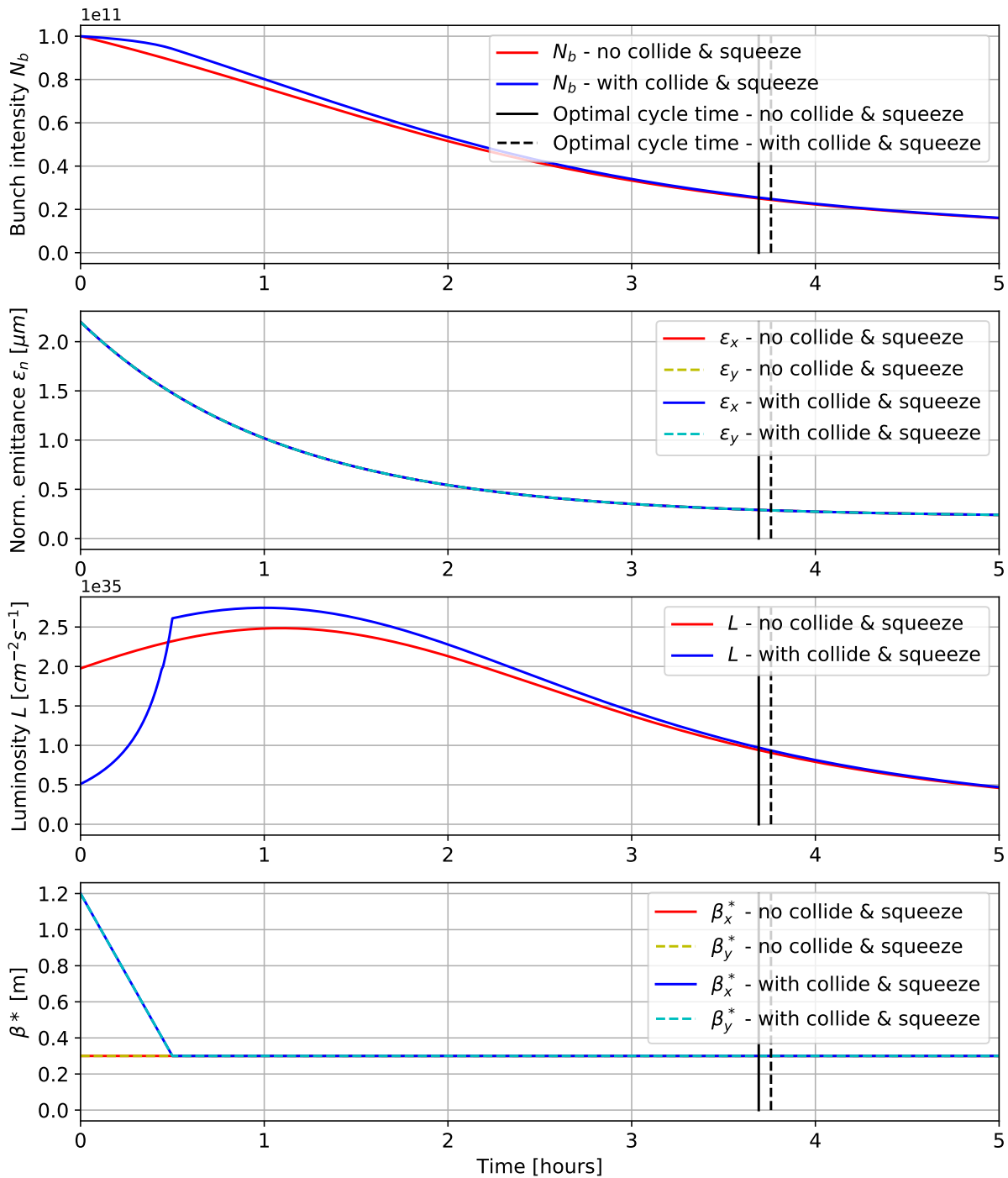
Figure 1: Beam parameters during FCC-hh physics fills with and without collide & squeeze.

2   MDI CONSIDERATIONS

Early studies of the final focus system layout concluded that the main contributor to the minimum β^* is the overall length of the triplet, while the L^* plays a minor role [1, Sec. III D]. This led to a clear strategy to minimize β^* with significant amounts of shielding reducing the free aperture of the final focus magnets: to choose the smallest L^* that does not restrict the detector design and to increase triplet length until dynamic aperture or chromaticity become obstacles. In this strategy the machine-detector interface plays a key role as it defines L^*. A sketch of the detector region layout is shown in Fig. 3. While the detector has a total length of about 50 m, extending to 25 m on either side of the IP, the opening scenario requires a total cavern length of 66 m. During operation, the gap between detector and cavern wall will be occupied by the forward shielding that protects the detector from secondaries back-scattered from the TAS. The aperture in the 2 m thick wall between cavern and tunnel is equipped with a cast iron absorber to complete the forward shielding. The TAS, a 3 m long copper absorber that protects the final focus magnets from collision debris is located 35 m from the IP. With an additional space of 2 m reserved for vacuum equipment and for the end of the magnet cryostat, first quadrupole of the final focus triplet starts at $L^* = 40$ m.

The beam pipe at the IP is made of 0.8 mm thick beryllium and has an inner radius of 20 mm. This pipe extends to ± 8 m to either side of the IP and is followed by a beryllium cone with an opening angle of 2.5 mrad corresponding to $\eta = 6$. From 16 m from the IP on, the inner radius of the aluminium beam pipe is constant at 40 mm, this is necessary for the opening of the detector.
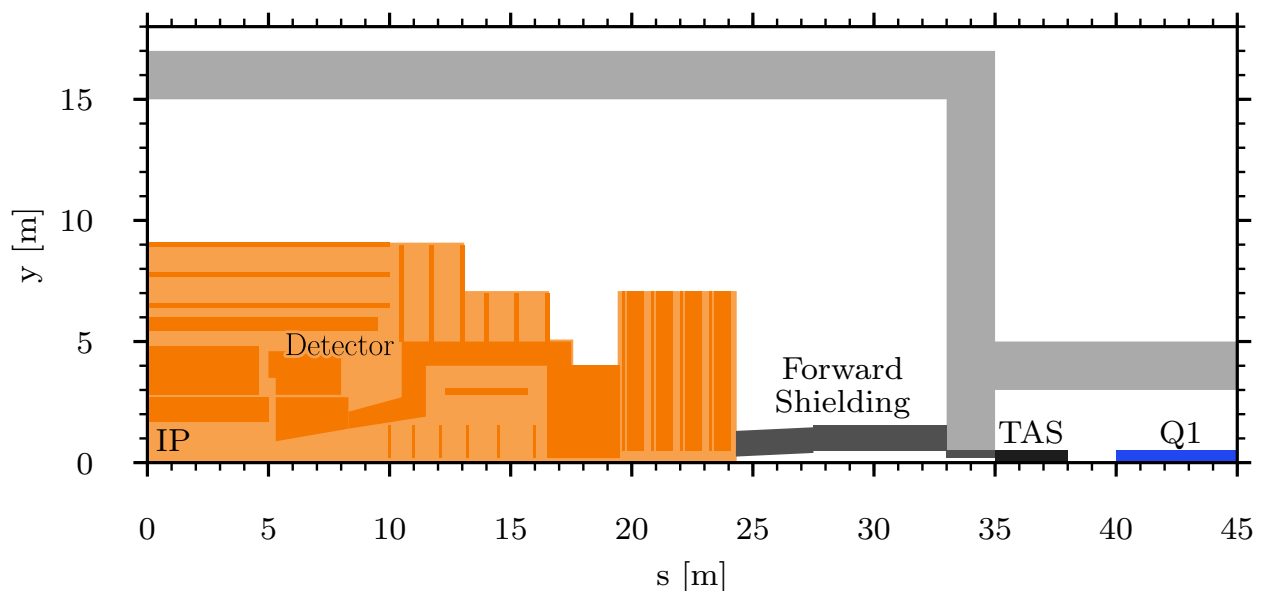

Figure 2: Detector and interaction region layout leading to the $L^* = 40$ m lattice. The IP is located at $(0, 0)$.

3   SYSTEM LAYOUT AND OPTICS

The interaction region layout of FCC-hh follows the same principles as the LHC and HL-LHC interaction regions. The layout is shown in Fig. 3. Starting at the Interaction Point (IP), the
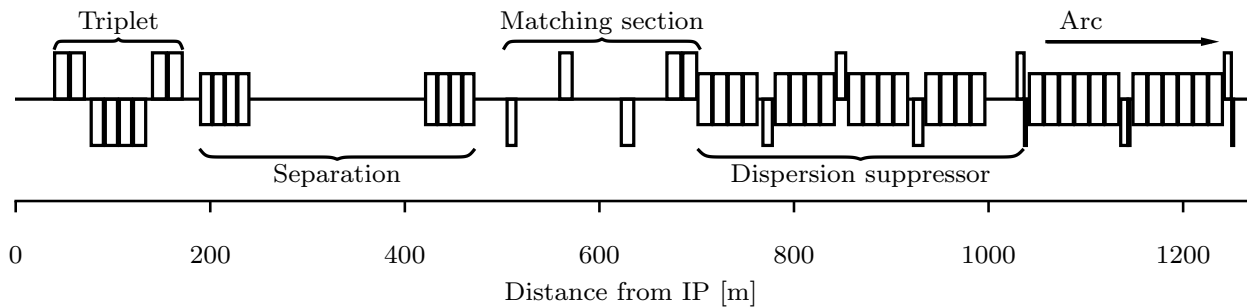

Figure 3: Layout of the high luminosity interaction region. The layout is antisymmetric around the IP at $(0, 0)$.

strongly focused and highly divergent beams pass a drift space with the length L^* chosen to accommodate the detector. Following this drift space, a final focus system comprised of three large aperture quadrupoles (hence called the triplet) focuses the beams in both the horizontal and vertical plane. The triplet consists of single aperture magnets that host both beams. The triplets on both sides of the IP are powered antisymmetrically. This has the advantage that the triplet region is optically identical for both beams. Behind the triplet, a shared aperture dipole D1 separates the two beams. After a drift, the double bore dipole D2 bends the separated beams onto parallel orbits again. The resulting reference orbits are shown in Fig. 4. Also depicted are orbit excursions that let the two beams collide with a crossing angle in order to avoid parasitic collisions outside the detector area. Four more quadrupoles Q4-Q7 make up the following matching section that occupies the rest of the straight section. The straight section is connected to the arcs by a two cell dispersion suppressor. To provide enough degrees of freedom to match all required beam parameters from the IP to the arcs, the four matching section quadrupoles, the three individually powered quadrupoles of the dispersion suppressor Q8-Q10 and well as three tuning quadrupoles in the first arc cell QT11-QT13 are used for the matching procedure.

3.1   FINAL FOCUS TRIPLET

The final focus design strategy calls for a long triplet in order to achieve small β^* values. In practice, not only chromaticity and dynamic aperture were limiting factors for the triplet length, but also the total length of the straight section that determines the arc side focal length of the final focus system, as well as the strength of the Q7 quadrupole. Furthermore the lengths of individual magnets must be equal or below 14.3 m in order to be compatible with a cryostat length of 15 m. The relative lengths of Q1, Q2 and Q3 were adopted from HL-LHC. As suggested in [4], Q1 was chosen to have a smaller aperture and higher gradient than Q2 and Q3 in order to minimize β^*. The specification for the triplet quadrupoles are listed in Table 10 and the layout
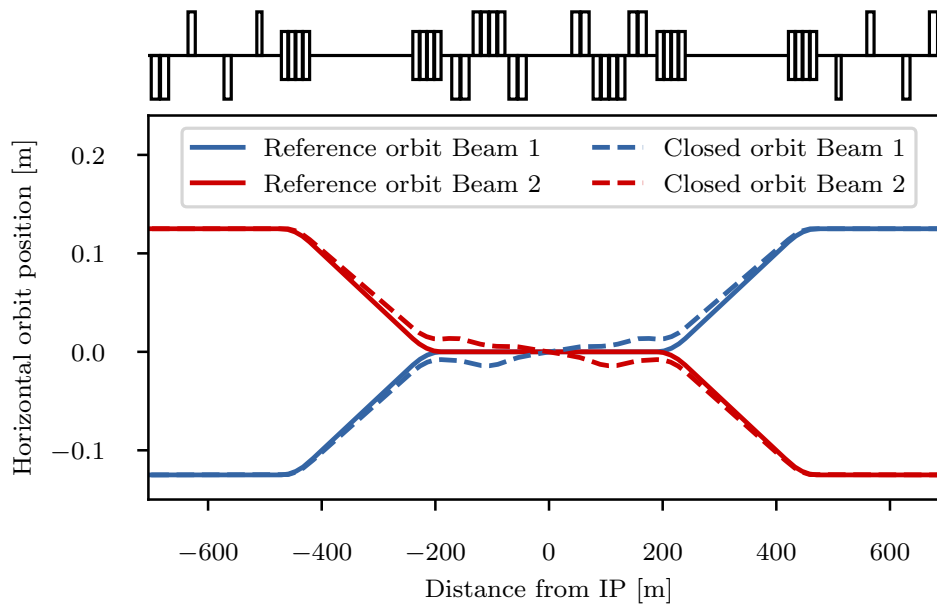
Figure 4: Reference orbits (solid lines) and closed orbits with crossing angles (dashed lines) in the interaction region.

of the final focus triplet shown in Fig. 5. Q1 and Q3 are made up of two submagnets each with length of 14.3 m. For the interconnects a drift space of 2 m is reserved between the submagnets. The drift between Q1 and Q2 as well as Q2 and Q3 is longer at 7 m and must house orbit correctors, BPMs and vacuum equipment. Q2 consists of four 12.5 m long submagnets. This not only allows for a similar length ratio as in the HL-LHC but also to place orbit correctors in the cryostat of the outermost Q2 magnets. Behind Q3, 18.8 m of space are reserved for higher order multipole correctors to compensate triplet field errors.
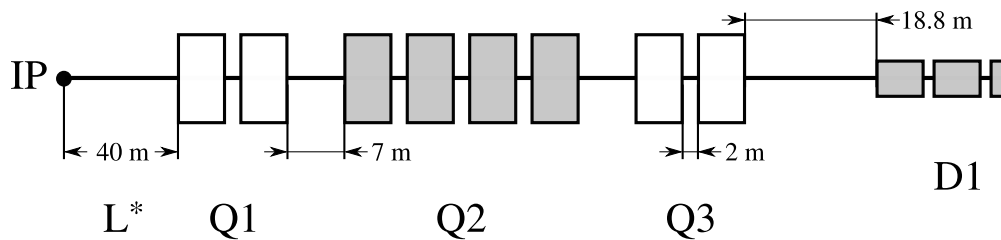
Figure 5: Layout of the final focus triplet.

A 35 mm thick inner shielding of INERMET180 protects the triplet magnets from collision debris. Furthermore the free aperture is reduced by a gap for the liquid helium for cooling (1.5 mm), the Kapton insulator (0.5 mm), a beam screen (2.05 mm), a gap for the insulation of the beam screen (2.0 mm) as well as the cold bore that scaled with 2.72 % of the coil aperture diameter, all of which have been modeled as simple layers. Despite this significant reduction of the free aperture, the triplet can accommodate a beam with lower than ultimate β^*. Figure 6 shows the β functions and horizontal dispersion in the EIR and Fig. 7 the corresponding aperture

Figure 6: Optics of the main interaction region with $\beta^* = 0.3$ m.
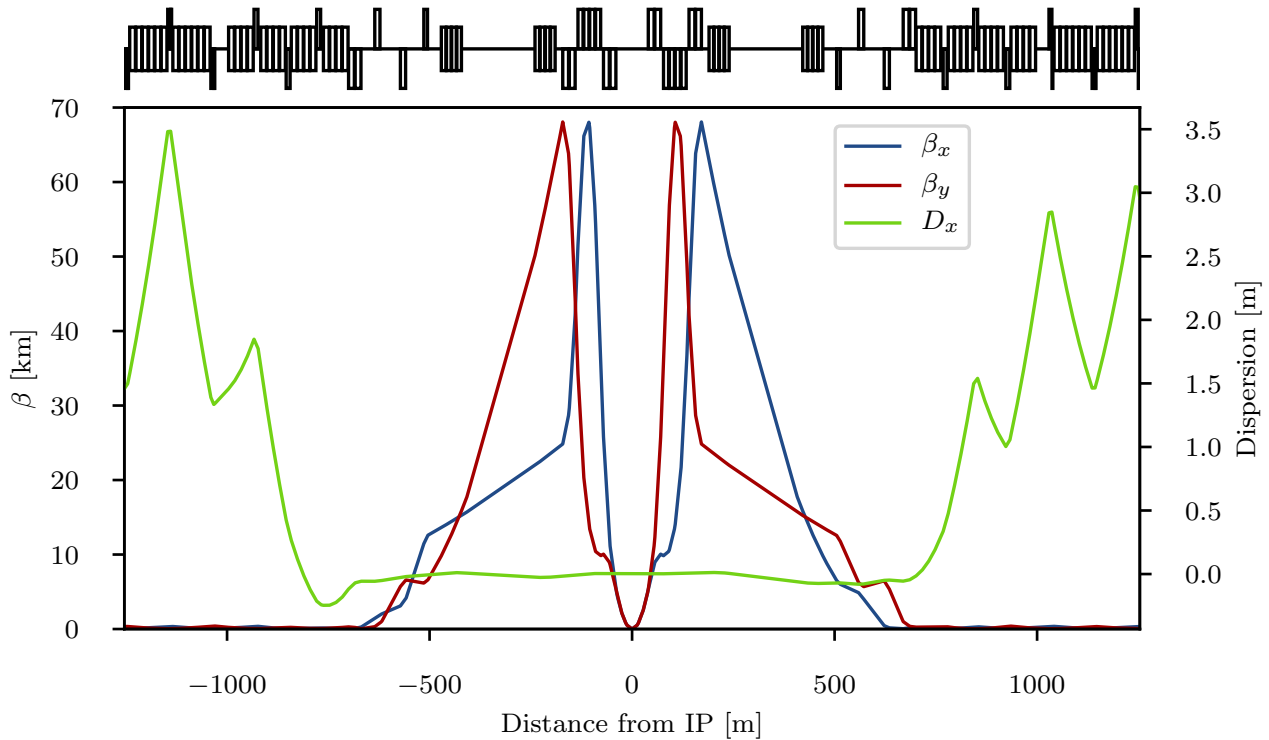
usage (without alignment tolerances). The beam stay clear is depicted in Fig. 8 showing a significant margin in terms of aperture. In fact, optics with almost $\beta^* = 0.2$ m can be achieved, although the chromaticity correction will not suffice with the current arc layout.

The maximum strength achievable by the sextupoles in the arcs has been estimated to be around 7529 T/m^2 [5], equivalent to 0.045 m^{-3}. As illustrated in Fig. 9a this strength is enough to correct for the cases with β^*=30 cm, but not for the beyond ultimate case with β^* =20 cm. For completeness Fig. 9a also includes the β^* =15 cm case possible in early designs but not compatible with the current thick shielding inside the final focus triplet quadrupoles. From the sextupole strength the maximum natural chromaticity that the sextupoles in the arcs are able to correct has been estimated to be around 557 units, as illustrated in Fig. 9b.
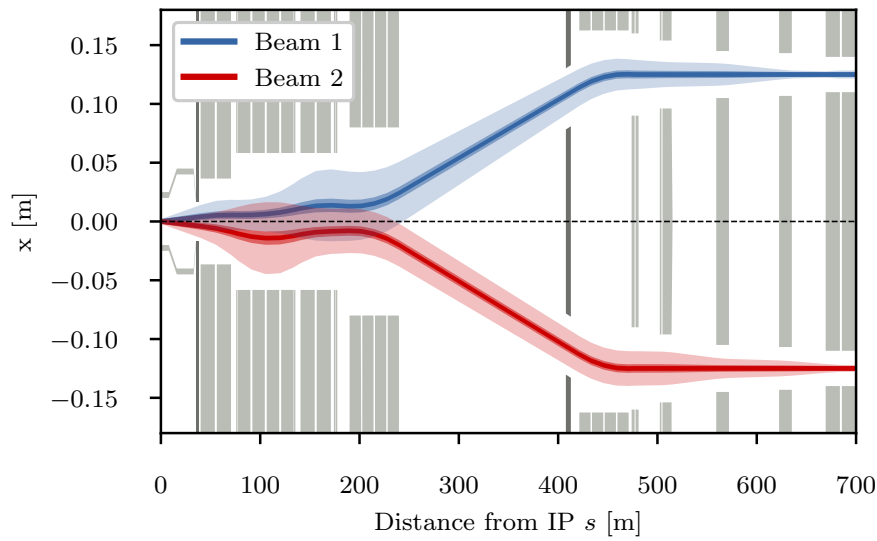
Figure 7: Overall layout of the insertion region between the IP and Q7. For each beam, the closed orbit, the $2\,\sigma$ envelope and the $15.5\,\sigma$ envelope for the ultimate β^* of $0.3\,\mathrm{m}$ are shown. The beam sizes include a β beating of $10\,\%$ and a closed orbit uncertainty of $2\,\mathrm{mm}$. Magnet apertures and the detector region beam pipe are illustrated with light gray while absorbers are shown in dark gray. The large aperture triplet magnets leave significant aperture margins.
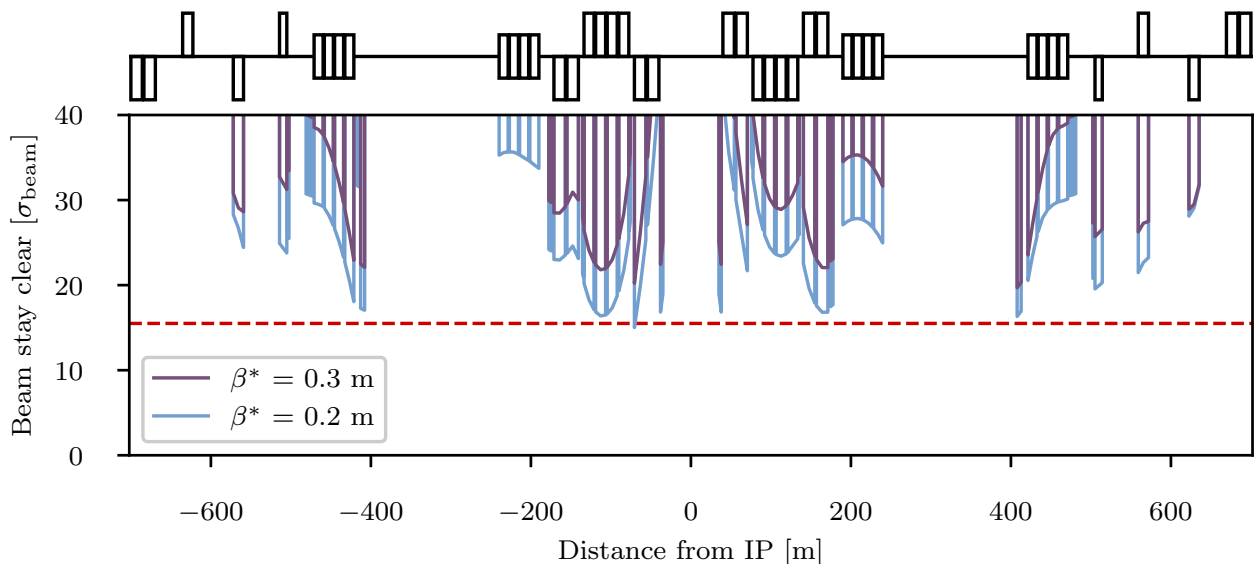
Figure 8: Beam stay clear of the high luminosity EIR for horizontal crossing and ultimate as well as beyond ultimate optics. For $\beta^* = 0.2\,\mathrm{m}$ the beam stay clear is just below the minimum of $15.5\,\sigma$ in the left Q1, suggesting a slightly larger β^* can be accommodated.
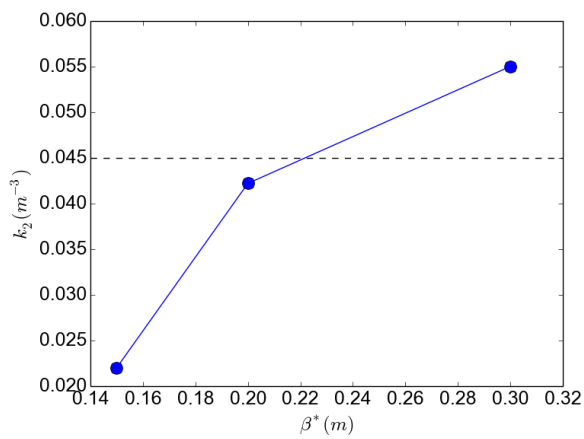
(a) *Absolute value of the defocussing sextupole strength for different β^*. The black dotted line indicates the maximum strength of the sextupoles.*
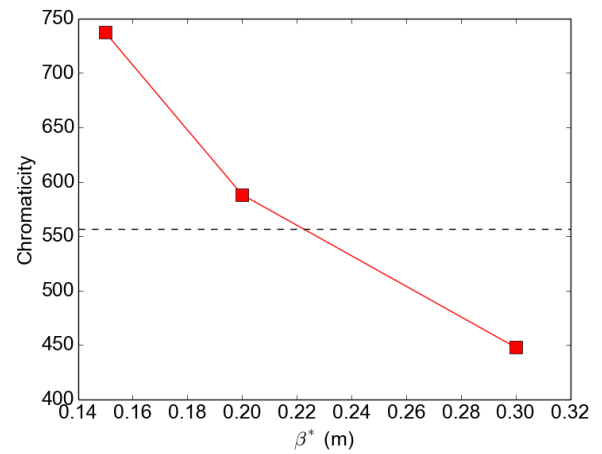
(b) *Absolute value of the vertical natural chromaticity for different β^*. The black dotted line indicates the maximum number of units that the system is able to correct.*

Figure 9: *Limits of the chromaticity correction*
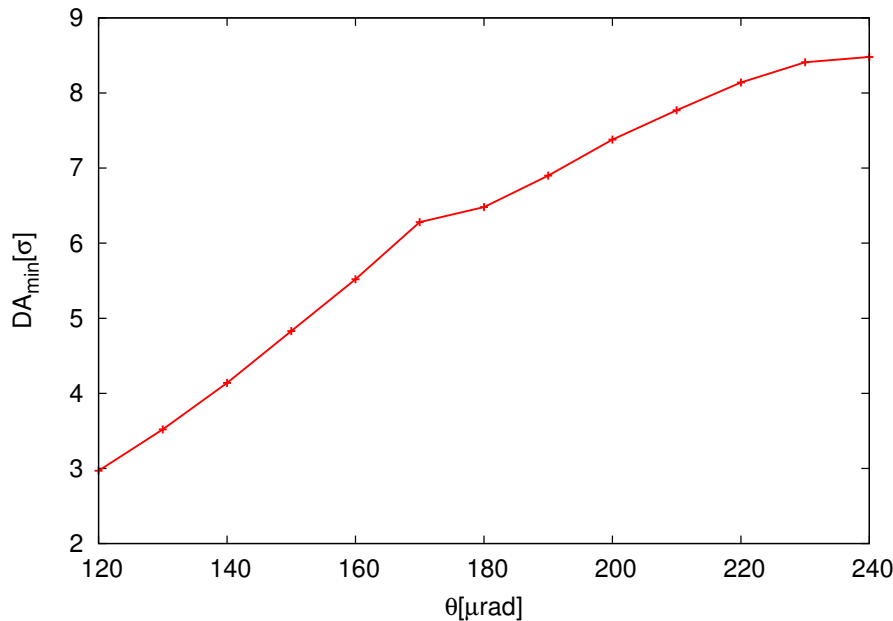
Figure 10: Dynamic Aperture in the presence of beam-beam interactions as a function of the crossing angle at the Interaction Point for the Ultimate collisions optics with $\beta^* = 0.3\,\mathrm{m}$ and $L^* = 40\,\mathrm{m}$ [6]

.

3.2 BEAM-BEAM EFFECTS AND CROSSING ANGLE

The beam-beam interaction can limit the performance of a particle collider. In fact, the beam-beam interaction can induce particle losses, resulting in a reduction of the beam lifetimes and can create a high background for physics experiments. In addition, the beam-beam interaction can be responsible for an elevated heat and radiation load on the collimation system, can induce emittance blow-up and can cause coherent beam instabilities with a consequent reduction of the luminosity reach. The design of FCC-hh is based on the LHC beam-beam theoretical studies and experience [7, 8, 9, 10]. As for the LHC and the HL-LHC, an alternating crossing scheme is chosen for the two high luminosity experiments in IPA and IPG, in order to passively compensate for tune and chromaticity shifts for PACMAN bunches [11]. Two additional, lower luminosity experiments are located in IPB and IPL. Assuming that the four experiments operate in proton-proton collisions with 25 ns bunch spacing, 352 long range interactions are expected.

Detailed beam-beam studies have been carried out by means of weak-strong as well as strong-strong models by using the SixTrack [12, 13] and COMBI [14, 15, 16] codes. The SixTrack code has been used for the computation of the area of stable motion in real space, the Dynamic Aperture (DA). A detailed lattice description and the LHC experimental data have been employed for the benchmark of the SixTrack code with and without beam-beam effects [17, 18]. The COMBI code makes use of a self-consistent treatment, including a simplified lattice description, and provides the evolution of macroscopic beam parameters, such as, the beam intensity and the emittance together with the Landau damping of coherent beam instabilities [10, 19]. For the DA studies presented here, the approach used is similar to the LHC and HL-LHC design studies [20, 21]. The LHC observations have shown that below a simulated DA of 4 σ a reduc-
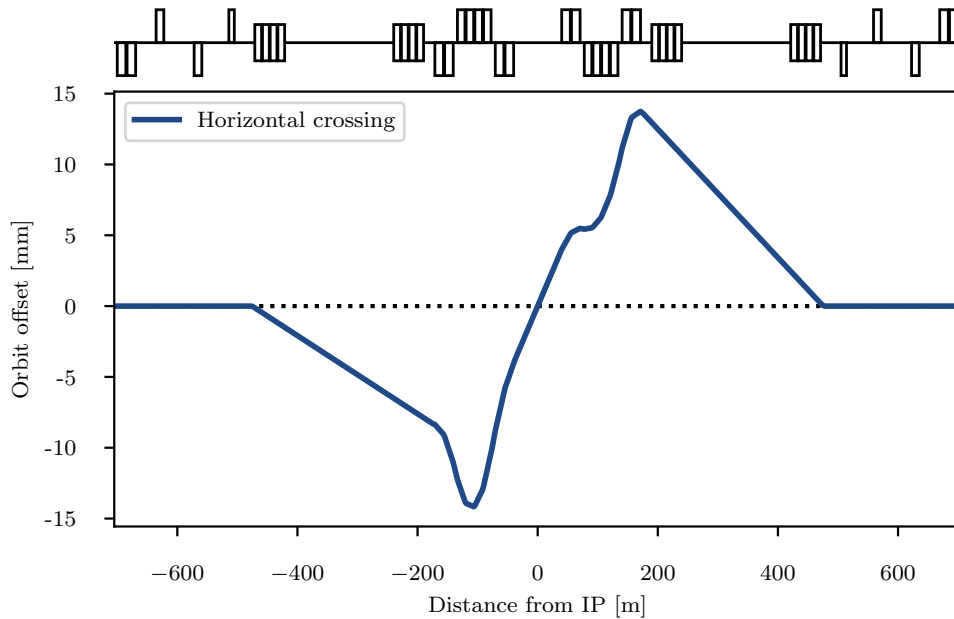
Figure 11: Orbit bump for a 200 µrad *horizontal crossing angle required at* $\beta^* = 0.3\,\text{m}$.

tion of beam lifetime starts to appear [7]. As described in [17, 22] a strong correlation exists between the beam intensity lifetime and the simulated DA for different beam configurations with and without beam-beam interactions. As it is shown in Fig. 10, a DA of 7.2 σ is ensured with a crossing angle $\alpha_c = 200$ µrad in IPA and IPG for the nominal normalized emittance of $\epsilon_n = 2.2$ µm and at the Ultimate β^* of 0.3 m. The corresponding orbit bump is shown in Fig. 11 and the beam-beam long range separations at the IR are shown in Fig. 12. For the Ultimate scenario with $\beta^* = 0.3$ m and the chosen crossing angle of 200 µrad (the blue dots), the long range separation at the first encounter is 17 σ. At this separation, the value of DA (7.2 σ) is well above 4 σ providing sufficient margin to avoid additional particle losses on the collimation system due to beam-beam diffusive mechanisms (including a relative momentum deviation of 10^{-4}). In addition, margins are also left for high chromaticity operations (up to 20 units) if required for mitigation of coherent beam instabilities, for operating in the presence of multipolar lattice errors [23] or to also collide in IPB and IPL. For the Baseline scenario with collisions at $\beta^* = 1.1$ m, the long range beam-beam separation is well above 30 σ at the first encounter (the red dots).

The DA as a function of the crossing angle in IPA and IPG for PACMAN bunches is shown in Fig. 13 (the blue and the green lines) for the H-V alternating crossing scheme. The red line corresponds to Nominal bunches. As visible, the DA for PACMAN bunches is always above the DA for Nominal bunches. The PACMAN effects of tune and chromaticity shifts do not have a significant impact assuming the passive compensation with alternating crossing planes in IPA and IPG [24].

The two-dimensional tune footprints at the end of the betatron squeeze before the beams are brought into collision are shown in Fig. 14, both for the Ultimate scenario (the green color) and for the Baseline scenario (the red color). For comparison, the tune spread provided by the
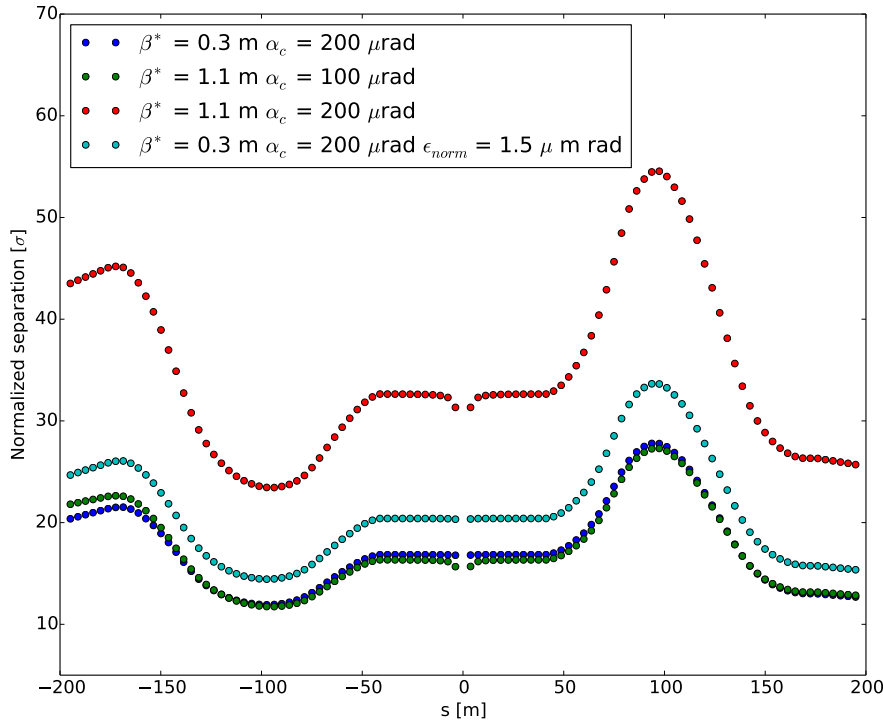
Figure 12: Beam-beam long range separations in the IR for the Ultimate $\beta^* = 0.3$ m with a crossing angle $\alpha_c = 200$ µrad and the nominal normalized emittance $\epsilon_n = 2.2$ µm (blue dots) and for a reduced normalized emittance of $\epsilon_n = 1.5$ µm rad (light blue dots). The beam-beam long range for the Baseline scenario for $\beta^* = 1.1$ m are also plotted with a crossing angle $\alpha_c = 200$ µrad (red dots) and with a reduced crossing angle $\alpha_c = 100$ µrad (green dots). For this last cases the nominal normalized emittance of $\epsilon_n = 2.2$ µm has been considered.

Landau octupoles, powered with their maximum strength and negative polarity, is also shown (the blue color). As expected, the long range contribution to the tune spread for the Baseline scenario with collisions at $\beta^* = 1.1$ m is negligible due to the beam-beam long range separations above 20 σ (the red dots in Fig. 12) and the tune footprint results to be the same as the one provided by the Landau octupoles only. The "Collide & Squeeze" has been proposed in order to maximize the beam stability at the end of the betatron squeeze with negative octupole polarity [25]: Collisions at $\beta^* = 1.1$ m are foreseen to avoid the reduction of the tune spread, and therefore of the Landau damping, that would occur at the end of the betatron squeeze to $\beta^* = 0.3$ m without collisions. If no coherent instabilities are observed, a reduction of the crossing angle at $\beta^* = 1.1$ m is possible down to a minimum value of 100 µrad. In fact, for this value of the crossing angle a DA of ≈ 7 σ is still preserved since the beam-beam long range separations (the green dots in Fig. 12) are the same as the Ultimate case with a crossing angle of 200 µrad (the blue dots in Fig. 12).

The beam parameters of the "Collide & Squeeze" scheme, together with the luminosity
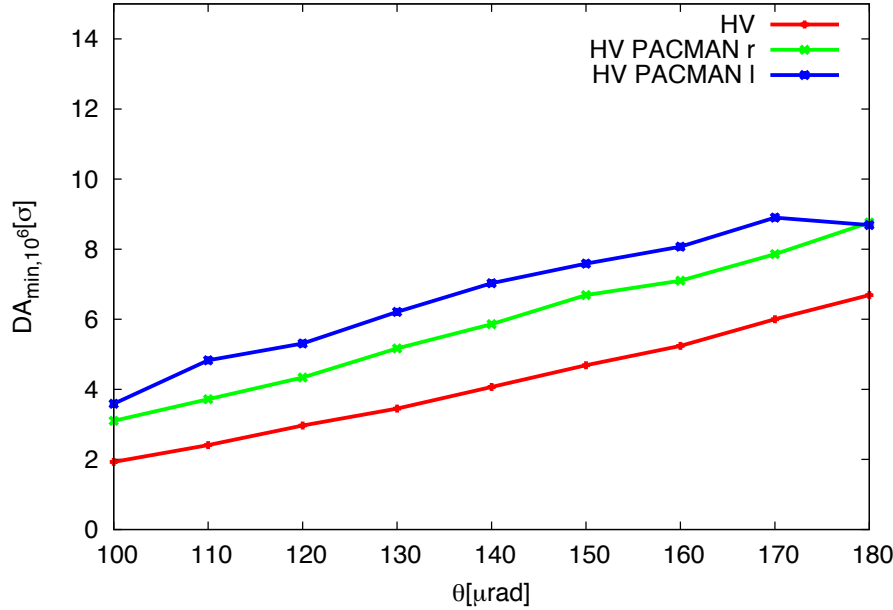
Figure 13: Dynamic Aperture, evaluated over 10^6 turns, as a function of the crossing angle in IPA and IPG for H-V alternating crossing scheme for Nominal bunches (the red line) and for PACMAN bunches (the blue and the green line) [23].

evolution, are shown in Fig. 1 as function of time. When the Ultimate $\beta^* = 0.3$ m is reached the normalized emittance is reduced to $\epsilon_n = 1.5$ µm due to synchrotron radiation, as shown in Fig. 1. The corresponding beam-beam long range separations are also shown in Figure 12. As expected the long range beam-beam separation at the first encounter is larger w.r.t. the Ultimate case and it is about 20 σ (the light blue dots).

In order to keep the impact of the two low luminosity experiments IPB and IPL in the shadow of the two main ones, a crossing angle of 180 µrad is required for the $\beta^* = 3$ m optics. As visible in Fig. 15 a DA is above 6 σ is expected for such configuration.

The total beam-beam tune shift for two head-on collisions in IPA and IPG will be $Q_{bbho} = 0.011$, as also visible in Fig. 16, where the two dimensional tune footprints with two head-on collisions in IPA and IPG are shown for the Baseline scenario with $\beta^* = 1.1$ m (the green color) and for the Ultimate scenario with a reduced normalized emittance $\epsilon_n = 1.5$ µm rad (the blue color) in order to take into account the effect of the synchrotron radiation shown by the emittance reduction in Fig. 1 at the end of the "Collide & Squeeze". For the case with the reduced normalized emittance ($\epsilon_n = 1.5$ µm) the total head-on beam-beam tune shift increases up to 0.016 (the blue color in Fig. 16). Since the total beam-beam tune shift Q_{bbho} is limited to be less than 0.03 [11, 26, 27, 28] the two low luminosity experiments IPB and IPL are required to operate with a transverse offset resulting in a maximum tune shift of $1 - 2 \times 10^{-3}$. However if the total beam-beam tune shift approaches the value of 0.03 and it is not tolerated, mitigations can be applied such as the blow-up of the emittance with controlled noise.
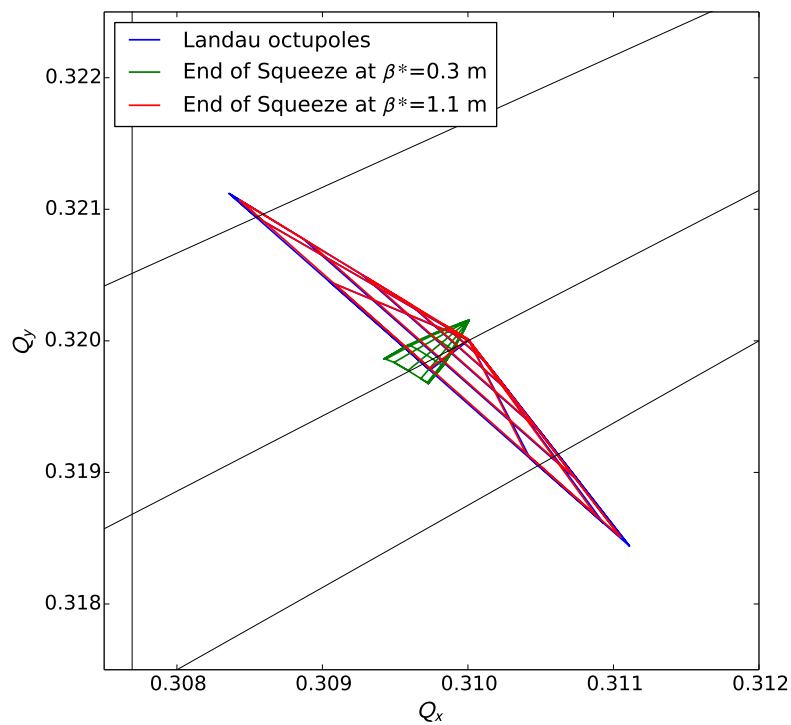
Figure 14: *Two-dimensional tune footprints at the end of squeeze including beam-beam interactions and Landau octupoles powered with negative polarity, for the Ultimate scenario (green color) and for the Baseline scenario (red color). For comparison the case with only Landau octupoles powered with negative polarity (maximum strength) is also shown (blue color).*
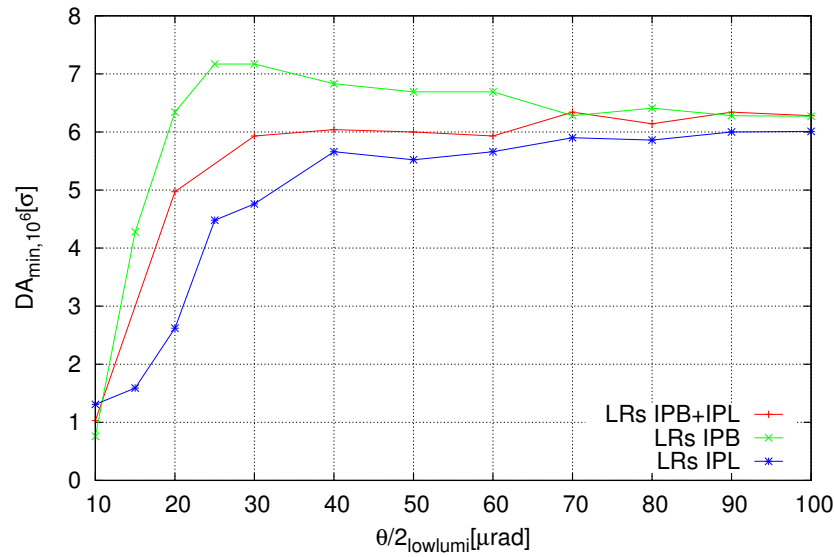
Figure 15: Dynamic Aperture, evaluated over 10^6 turns, as a function of the half crossing angle at IPB and IPL, including beam-beam long range interactions in IPB only (the green line), in IPL only (the blue line) and in both IPB and IPL (the red line) [23].
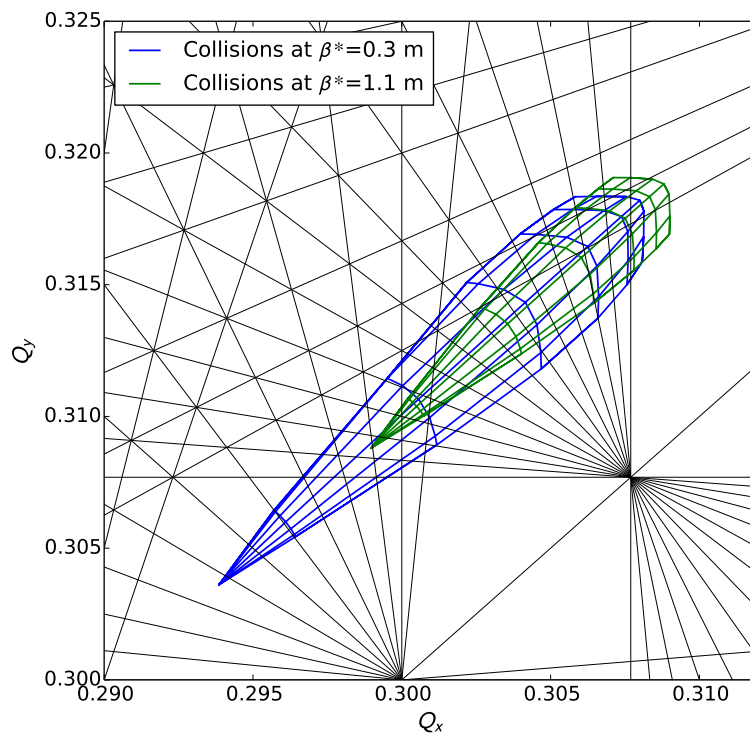
Figure 16: Two-dimensional tune footprints with head-on collisions in IPA and IPG for the Baseline scenario with $\beta^* = 1.1\,\mathrm{m}$ (green color) and for the Ultimate scenario $\beta^* = 0.3\,\mathrm{m}$ with a reduced normalized emittance $\epsilon_n = 1.5\,\mathrm{\mu m\ rad}$ (blue color).

3.3 DYNAMIC APERTURE WITH TRIPLET ERRORS

Dynamic aperture (DA) studies were performed using SixTrack on a thin-lens version of the FCC-hh lattice and errors in both the arcs and the triplet. Concerning the magnetic imperfections of the triplet 60 different realisations (seeds) have been used. These errors are given in the following form [29]:

$$b_n = b_{nS} + \frac{\xi_U}{1.5} b_{nU} + \xi_R b_{nR},$$

(1)

with b_{nS}, b_{nU} and b_{nR} referring to the main, uncertainty and random components, and both ξ_U and ξ_R are Gaussian distribution random variables cut at 1.5 a 3 σ respectively; ξ_U changes from seed to seed but remains the same for all magnets of the same class while ξ_R changes also from magnet to magnet. The magnetic field in the magnets is then given as:

$$B_y + iB_x = B_{\text{ref}} \sum_{n=1}^{N} (b_n + ia_n) \left(\frac{x + iy}{R_{\text{ref}}} \right)^{(n-1)}.$$

(2)

The errors for the triplet of the FCC have been based on the error table for the HL-LHC triplet [30] but adapted to the FCC magnets by scaling the reference radius proportionally to the corresponding magnet aperture. In the absence of a magnet design this approach seems sensible as the HL-LHC triplet magnets already use Nb$_3$Sn technology. The nonlinear terms affecting the beam stability derived from these magnets will change with respect to the HL-LHC depending on the new aperture and β function at their location [31]. The field error tables used in the dynamic aperture studies are listed in the hardware specification, Section 9, in the Tables 11 and 12 for the triplet quadrupoles and Tables 14 and 15 for the separation and recombination dipoles.

Non-linear errors in the triplet quadrupoles have a severe impact on the single particle stability. Therefore, DA studies at collision energy with errors on the triplet and crossing angle proved to be challenging. Several corrections were implemented to compensate for the reduction on DA, but it was found that at collision energy two corrections were particularly important to achieve a DA above the target: optimizing the phase between the main IRs (IRA and IRG) and the implementation of non-linear correctors in the IR, to minimize the resonance driving terms arising from the errors in the triplet.

The minimum DA vs β^* at collision energy with errors on both the arcs and the triplets, and with and without non-linear correctors is shown on Fig. 17. The non-linear correctors include two sextupoles (normal and skewed) and two octupoles (normal and skewed) behind each triplet. A significant increase is observed on all cases when adding the non-linear correctors, except for the case with β^*=1.1 m whose DA is already large without non-linear correctors. The ultimate case with β^*=0.3 m shows a DA above the target of 10 σ even without non-linear correctors, by optimizing the phase advance and other corrections; however, the use of non-linear correctors is still recommended in case other errors affect the DA (like beam-beam). Furthermore, as shown in the figure, the use of non-linear correctors become essential for cases with β^* <0.3 cm.

The DA was also computed for the case with flat beams (design in Section 6). The DA for this case gave similar results as the case with $\beta^* = 30$ cm and round beams, with a DA above 10 σ without non-linear correctors (11.6 σ), increasing to 24.6 σ when the non-linear correctors were included.
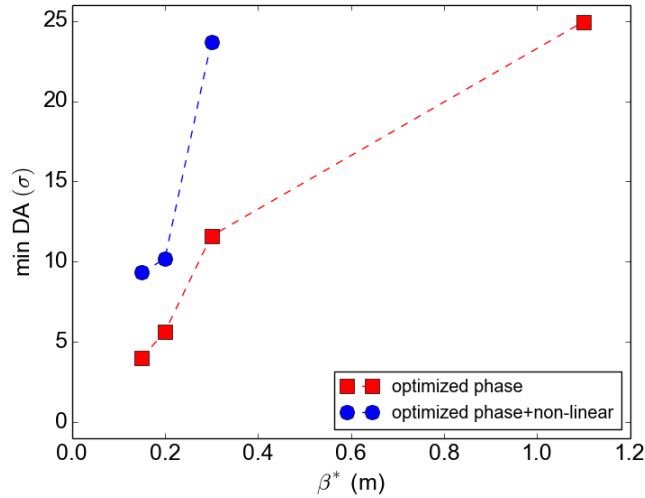
Figure 17: Minimum DA over 60 seeds versus β^* with and without non-linear correctors.

Table 2: Crossing angle and luminosity reduction due to crossing angle for different collision optics.

Optics version	β^* [m]	Full crossing angle [µrad]	Luminosity reduction factor
baseline	1.1	104	0.85
ultimate	0.3	200	0.40
beyond ultimate	0.2	245	0.28

3.4 CRAB CAVITIES

In the long shared aperture section around the IP, the two counterrotating beams are separated by an orbit bump in order to avoid parasitic crossings. The two beams only cross each other at the IP with a crossing angle θ. The crossing angle determines the separation of the beam in the shared aperture and thus the long range beam-beam effect. The minimum crossing angle was determined by beam-beam studies to be $200\,\mu\mathrm{rad}$ for the ultimate β^* of $0.3\,\mathrm{m}$ and then scaled for other optics to provide the same normalized separation of $\approx 17\,\sigma$. Table 2 list the crossing angle for a set of collision optics together with the luminosity reduction factor caused by the reduced geometric overlap of the bunches at the IP due to the crossing angle. For ultimate optics and beyond, FCC-hh is not able to provide even half of the luminosity head-on would provide. It is clear that the luminosity reduction in the high luminosity EIRs must be compensated by crab cavities.

Initial studies with crab cavities show that a crab voltage of $13.4\,\mathrm{MV}$ per beam on either side of each high luminosity IP is needed to provide full crabbing in ultimate optics, corresponding to $107.2\,\mathrm{MV}$ in total. Half of this voltage must be horizontally deflecting in one EIR, the other half vertically deflecting in the other EIR. For optics beyond ultimate parameters, the crab voltage increases up to $8 \times 18.1\,\mathrm{MV}$. Orbit leakage of the crab orbit into the arcs varied strongly during the evolution of the lattice. In the latest lattice version it appears to be small, causing only small orbit aberrations in the other IPs. More detailed studies should be performed to get a
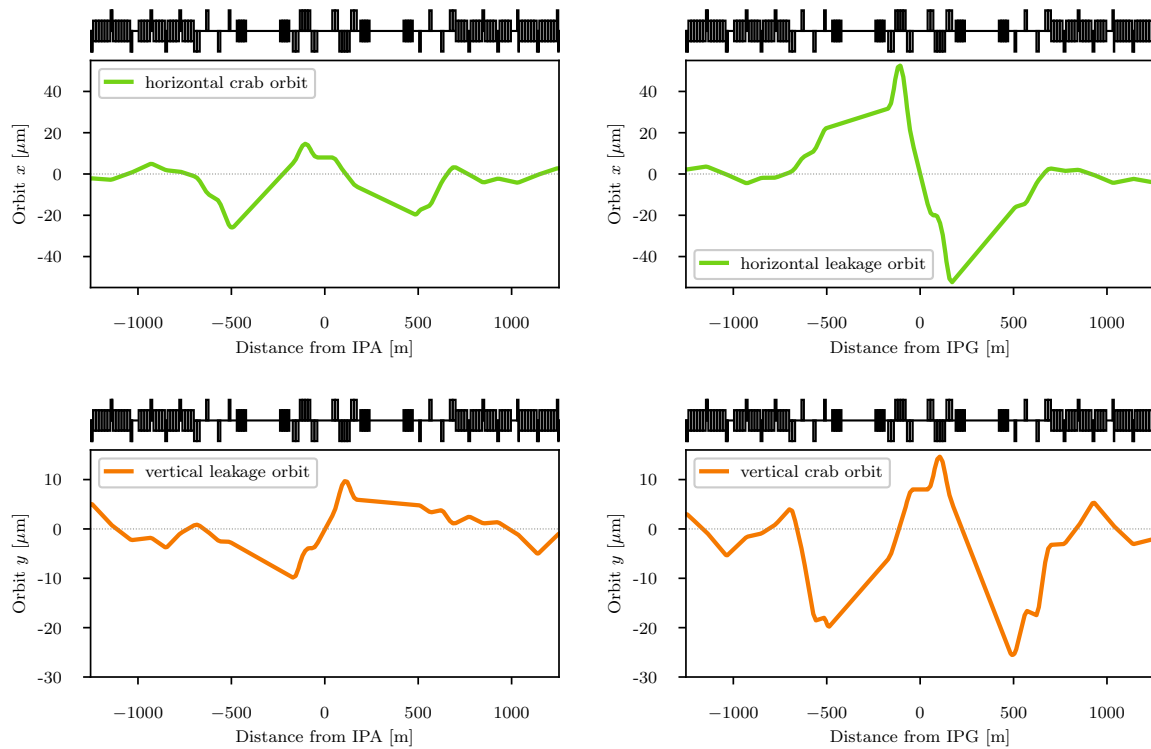
Figure 18: Crab orbits for $\beta^* = 0.3\,\mathrm{m}$ and orbit leakage into the other high luminosity EIR.

better control of the orbit leakage in the future. The crab orbits and orbit leakage into the other high luminosity EIR are shown in Fig. 18 for ultimate optics.
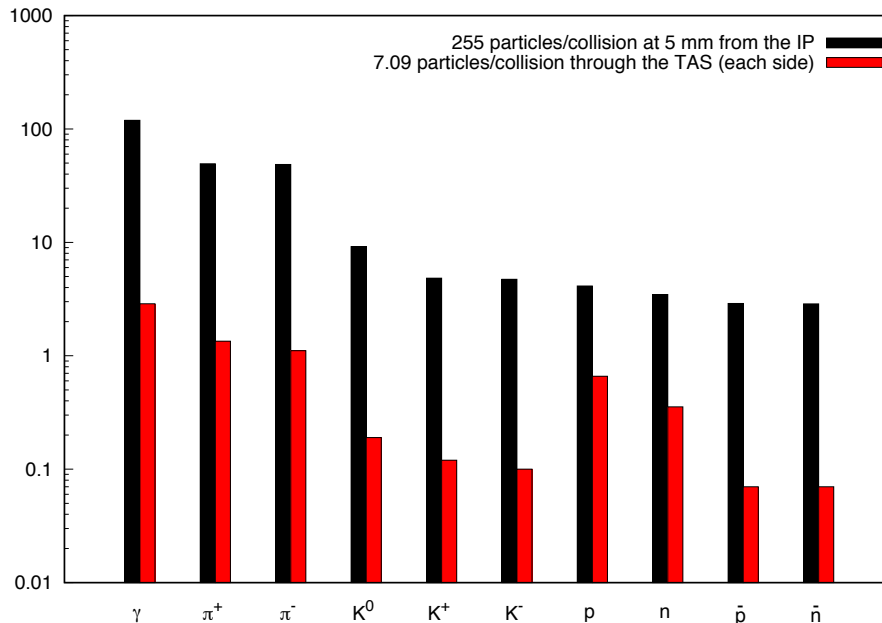
Figure 19: Collision debris from a single 100 TeV c.m. proton-proton inelastic reaction at 5 mm from the interaction point (black) and at the exit of the TAS (red) at 35 m from the IP.

4   ENERGY DEPOSITION FROM COLLISION DEBRIS

Proton-Proton inelastic collisions taking place in the FCC-hh, particularly in the two high luminosity detectors, generate a large number of secondary particles. Moving away from the Interaction Point (IP), this multiform population evolves even before interacting with the surrounding materials due to the decay of unstable particles, such as neutral pions which decay into photon pairs. Most of these particles are intercepted by the detector and release their energy within the cavern. However, the most energetic particles, emitted at small angles with respect to the beam direction, travel farther inside the vacuum chamber and reach the accelerator elements, causing a significant impact on the magnets along the Experimental Insertion Region (EIR), particularly in the final focusing quadrupoles and the separation dipoles. Fig. 19 shows the particle population close to the interaction point and at the exit of the TAS: the average multiplicity of a single 100 TeV c.m. proton-proton inelastic interaction is ∼255. At ultimate instantaneous luminosity conditions ($30 \times 10^{34} cm^{-2} s^{-1}$) the power released toward each side of the IP is 260 kW, that is impacting upon the FCC-hh elements and consequently dissipated in the machine, the nearby equipment (e.g. electronics racks), and the tunnel walls. It is important to study how these particles are lost in order to implement the necessary protections for shielding sensitive parts of the machine and in particular of the magnets.

In this context, Monte Carlo simulation of particle interaction with matter plays a crucial role relying on a detailed implementation of physics model and an accurate 3D description of the region of interest. The FLUKA code [32, 33] is extensively used in this conceptual design study, based on the experience collected in the LHC and HL-LHC design [34] as well as the benchmarks

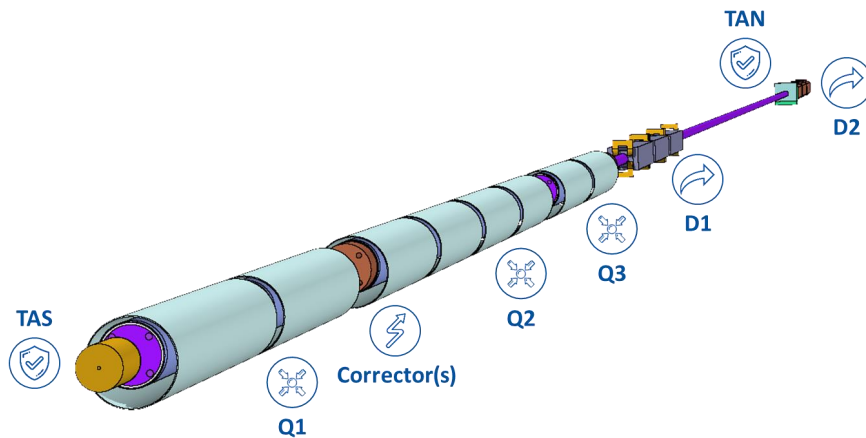*Figure 20: 3D rendering of the FLUKA geometry of the EIR, including ∼700 m of beam line. The picture shows the first ∼500 m including the TAS, the inner triplet, the TAN, the separation and recombination dipoles D1 and D2.*

already available in literature for these machines [35]. Fig. 20 shows part of the FLUKA model of the EIR, for the latest layout available at the time of the simulation ($L^* = 40$ m) including 700 m of accelerator line with the inner triplet, the separation and recombination dipoles (D1 and D2), the Target Absorber Secondaries (TAS), the Target Absorber Neutrals (TAN), and the matching section (Q4-Q7). The following coil apertures (in diameter) were implemented in the model: Q1 (MQXC) 164 mm, Q2 (MQXD) and Q3 (MQXE) 210 mm, orbit correctors 210 mm, Q4 (MQY) 70 mm, Q5 (MQYL) and Q6 (MQYL) 60 mm, Q7 (MQM) 50 mm. The matching section quadrupoles include a rectellipse beam-screen modelled according to optics constraints. To protect the inner quadrupoles coils, a 35 mm thick tungsten shielding was implemented in the mechanical design of the triplet magnets and the orbit correctors: the shielding thickness reported in this study is the maximum allowed in order to comply with optics requirements. The first separation dipole, D1 (MBXW), is a single aperture warm dipole, with a pole tip aperture of 170 mm. The TAN, made of a 4 m long tungsten absorber, includes twin diverging apertures of 52 mm. D2 (MBRW) is a twin aperture warm dipole: each module has been modelled with two parallel bores centered at a separation distance varying from the first to the last, in order to reach on the non-IP side the arc value of 250 mm. Proton-proton collisions at 100 TeV c.m. with a vertical half crossing angle of 100 μrad have been simulated and the particle shower was tracked all along the accelerator elements [36, 37]. The study of the matching section requires an extreme computational effort to achieve a statistically meaningful outcome and therefore it is planned to be finalized at a later stage. Results concerning the triplet-D2 area are presented in the following.

The total power deposited in the cold magnets (Tab. 3) is shared between the cold mass and the massive tungsten shielding, with a ∼15-85 ratio. In particular, the Q1B (MQXC.B1RA) turns out to be the most impacted element of the triplet with a total power of about 2 kW in

Table 3: *Total power distribution in the EIR elements.*

Element	Total Power [kW]		
	Cold Shielding	Cold Mass	Warm Mass
TAS.RA			26.5
MQXC.A1RA	4.6	0.78	
MQXC.B1RA	13	1.92	
MCBXDHV.A2RA	0.06	0.06	
MQXD.A2RA	1.53	0.32	
MQXD.B2RA	0.7	0.09	
MQXD.C2RA	4.6	0.63	
MQXD.D2RA	5.93	0.81	
MCBXDHV.B2RA	0.51	0.05	
MQXE.A3RA	6.02	0.77	
MQXE.B3RA	7.8	0.95	
MCBXCHV.3RA	0.94	0.17	
MBXW.A4RA			4.99
MBXW.B4RA			3.57
MBXW.C4RA			3.57
MBXW.D4RA			3.96
TAN.4RA			107
MBRW.A4RA			0.07
MBRW.B4RA			0.01
MBRW.C4RA			0.003
MBRW.D4RA			0.002

the cold mass and 13 kW in the shielding.

Fig. 21 shows the absorbed power profile (in W/m) along the TAS-D2 region, where triplet cold mass and shielding contributions are added up. In the Q1B cold mass a linear power loss of ∼150 W/m is reached. On the other hand, a preliminary evaluation, based on the cooling capabilities of the beam-screen of the 16 T main dipoles, indicates that four helium tubes of 15 mm diameter, placed in a 45° pattern with respect to the mid planes, would allow to dissipate the 13 kW (∼0.8 kW/m) deposited in the Q1B shielding [37]. The possibility of a shielding mechanical design embedding such a cooling circuit is currently under investigation.

Fig. 22 shows the peak power density profile in the triplet quadrupole coils, reaching a maximum of 5 mW/cm^3 at the end of the Q1B that matches with no margin a first conservative estimate of the quench limit. Studies to better determine the latter are currently ongoing [38]. Recently, [39] showed that the 11 T Nb$_3$Sn HL-LHC dipoles are expected to withstand steady state loads ten times higher.

To estimate the integrated luminosity reach with respect to the insulator lifetime, the absorbed dose in the magnet coils was calculated. Fig. 23 shows the peak dose profile for the ultimate integrated luminosity goal (30 ab^{-1}). Assuming an operational limit of 30 MGy for conventional radiation resistant insulator materials, the most critical element (Q1B) exceeds it
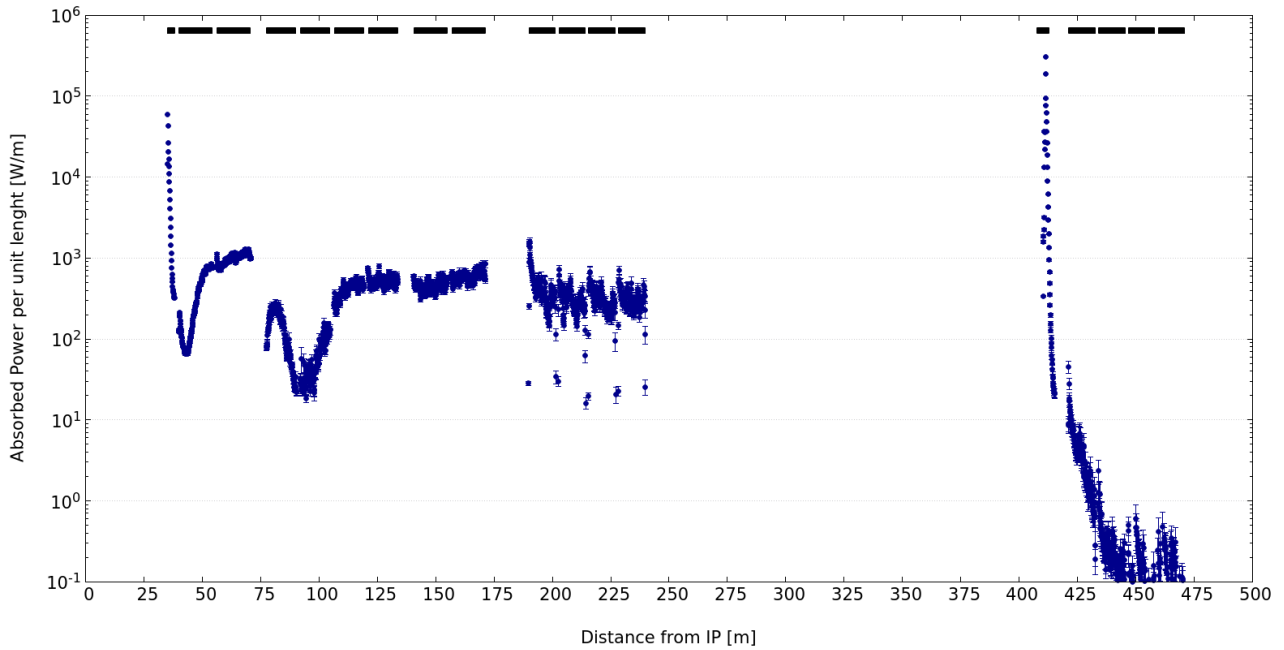
Figure 21: Absorbed power profile in the elements of the TAS-D2 region at the ultimate instantaneous luminosity of $30 \times 10^{34} cm^{-2} s^{-1}$.

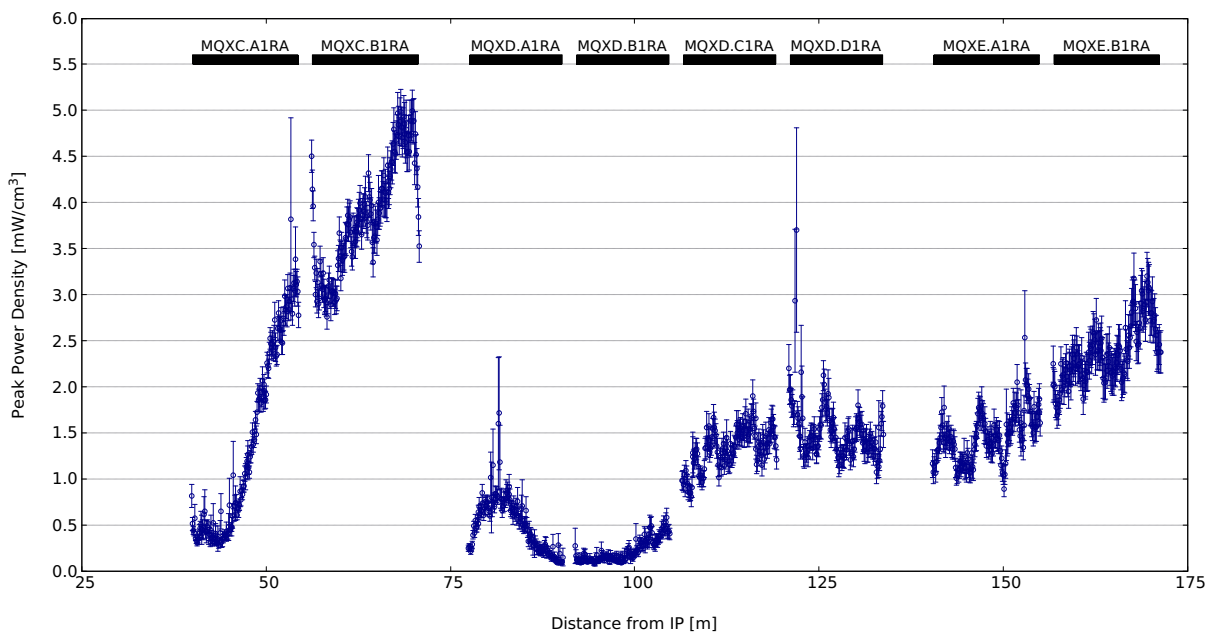*Figure 22: Peak power density profile in the triplet quadrupole coils at the ultimate instantaneous luminosity of $30 \times 10^{34} cm^{-2} s^{-1}$. Values are averaged over the radial cable thickness, with an azimuthal resolution of 2°. Vertical bars indicate the statistical error.*
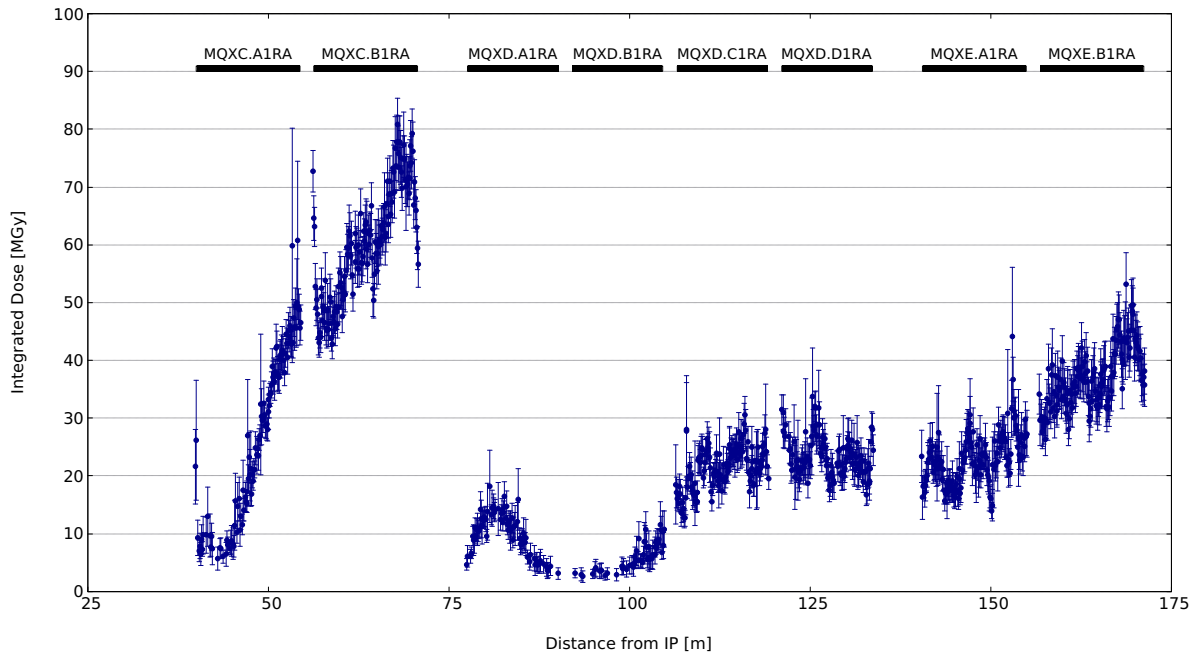
Figure 23: Peak dose profile in the triplet quadrupole coils for the ultimate integrated luminosity target ($30\,\text{ab}^{-1}$). Values refer to a radial and azimuthal resolution of $3\,\text{mm}$ and $2°$, respectively. Vertical bars indicate the statistical error.

by a factor 2.5. As previously mentioned, the model is already containing the maximum shielding thickness allowed by beam aperture requirements ($35\,\text{mm}$). Nevertheless, a Q1 split featuring a larger Q1B aperture at the price of a lower gradient, to be compensated in the Q1A, would allow a respective increase of the shielding thickness reducing the maximum dose. Moreover, crossing angle polarity and plane alternation are known to significantly reduce the maximum dose, by more equally distributing the radiation load in the coils [36]. Finally, the dose limit might be increased by using more radiation hard insulator, e.g. epoxy/cyanate-ester blends [38]. Alternatively, the replacement of the inner triplet once during the FCC-hh era might be considered.

With regard to the warm dipoles, the peak dose profile in D1 is reported in Fig. 24. Both D1 and D2 have been modelled without embedding any shielding but with a design moving the return coils far from the beam pipe, to reduce their exposure to the collision debris. This solution allows already for an important gain. However, the picture is rather similar to what was shown above for the triplet quadrupoles, with a peak dose in the first module (D1A) evaluated to be three times the $30\,\text{MGy}$ limit. In this case, a front mask as well as internal shielding can offer a substantial benefit. With regard to D2, the highest value expected at the D2A IP end is below $10\,\text{MGy}$, while peak doses ten times lower have been found in the D2C and D2D. Thanks to the protection provided by the TAN, the D2 presents no major concern for the coil insulator lifetime, even for the ultimate integrated luminosity target.

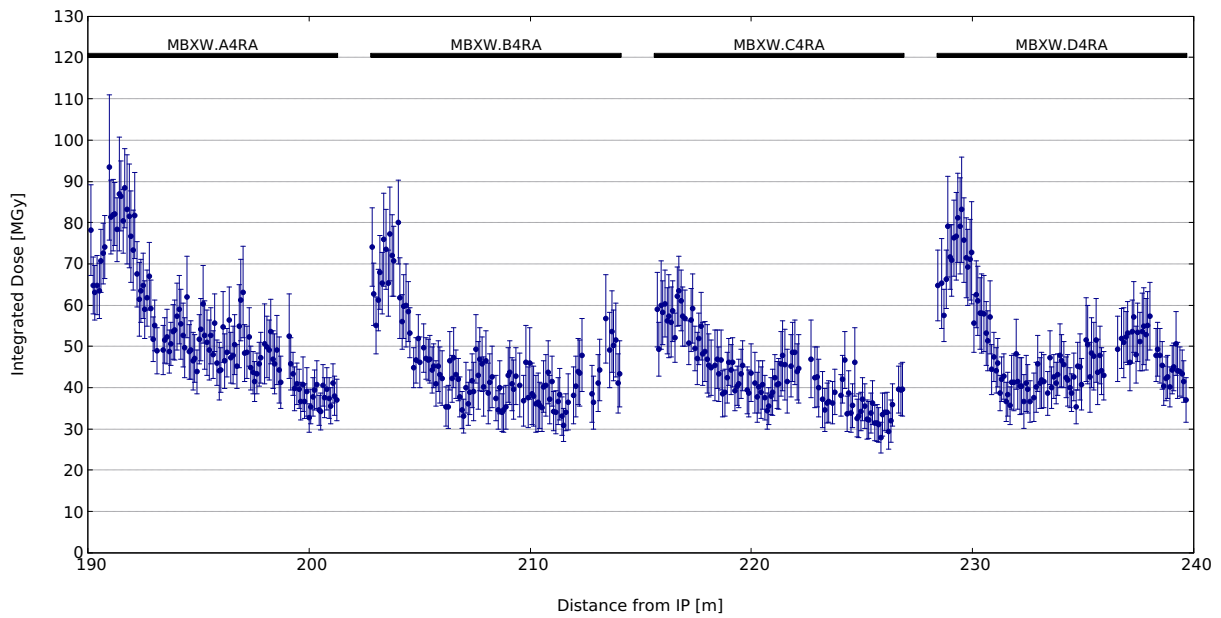*Figure 24: Peak dose profile in the D1 warm separation dipole coils for the ultimate integrated luminosity target ($30\,\mathrm{ab}^{-1}$). Values are averaged over a $3\,\mathrm{mm}$x$3\,\mathrm{mm}$ transverse area. Vertical bars indicate the statistical error.*

5 PHOTON BACKGROUND FROM SYNCHROTRON RADIATION

The amount of power radiated by Synchrotron Radiation (SR) strongly depends on the relativistic γ Lorentz factor of the moving particle, and thus on its energy to mass ratio: $P \propto \gamma^4 \rightarrow P \propto (E/m)^4$ [40].

Due to their mass, SR emitted by protons is usually a very small source of backgrounds in the experiments, even in very high energy proton beams such as LHC. However, in the case of FCC, in which beams are planned to reach 50 TeV of energy, also this possible source of background should be carefully evaluated.

The critical energy of the emitted SR scales with Lorentz factor γ and bending radius ρ according to γ^3/ρ. While the increase of FCC-hh center of mass energy with respect to the LHC is about a factor 7, the critical energy of emitted photons increases by a factor 100, shifting the energy spectrum from hard ultraviolet for LHC (which is easily absorbed) into soft X-rays of several keV for FCC. Since the Beryllium of the inner beam pipe can start to become transparent at these energies, some of these photons could traverse the beam pipe and may potentially constitute a background in the detectors.

To address this study, a dedicated software tool has been developed, validated and used. MDISim [41] is a toolkit that combines existing standard tools MAD-X [42], ROOT [43] and GEANT4 [44]. It reads the MAD-X optics files, and it uses its Twiss (and optionally Survey) output file to export the geometry and the magnetic field information in a format which can be directly imported in GEANT4 to perform particle tracking, including the generation of secondaries and detailed modelling of the relevant absorption processes.

The lattice named LATTICE_V9 has been used for this study, namely the baseline and ultimate optics, where β^* is 1.1 m and 0.3 m, respectively. The free length between the IP and the first quadrupole L* is 40 m. MDISim has been used to reconstruct the region from -700 m to 700 m around the Interaction Point A (IPA), see Figure 25 for a top view. The study also applies to the second interaction point named IPG, that has the same design and is located approximately 50 km away from IPA.

The beam pipe apertures upstream and downstream IPA are symmetrical. From IPA to ±8 m, the beam pipe is made of 0.8 mm thick Beryllium with an inner radius of 20 mm, representing a critical region due to its proximity to the vertex detector. The following 8 m are covered by a Beryllium cone with an opening angle of 2.5 mrad. From ±16 m to ±35 m respectively, the material is Aluminum and the beam pipe radius is 40 mm. The entire detector
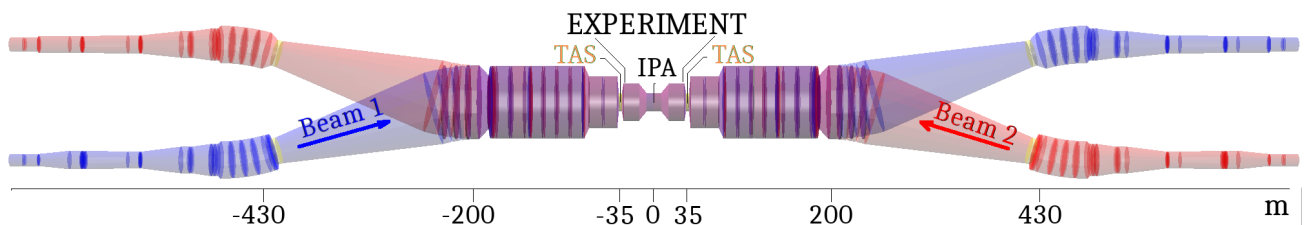

Figure 25: FCC-hh interaction region top view as resulting from MDISim, from -700 m to 700 m. The beam pipe is in blue for beam 1 and in red for beam 2. The transverse dimensions have been scaled up 500 times for visualization.
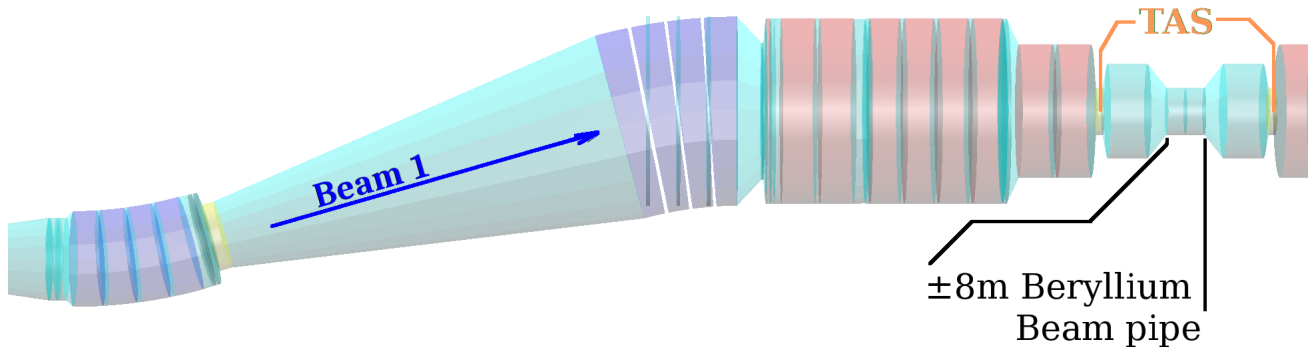
Figure 26: Top view of the beam pipe 3D-model obtained with MDISim. Dipoles are in violet, drifts in light blue, quadrupoles in orange, collimators in yellow.

layout occupies the region between ±25 m, followed by a forward shielding section from ±25 m to ±35 m. At ±35 m from the IPA, outside the detector and shield area, the Target Absorber Secondaries (TAS) is placed as absorber to protect the insertion quadrupoles from collision debris and its aperture radius is 20 mm. The aperture radii outside the region between the two TAS are larger than 56 mm, until the collimator TAN at ±412 m where it is reduced to 29 mm.

The dipoles in the experimental region shown in Figure 25 are 2 T magnets 11.3 m long, differently from the nominal arc dipoles which are 16 T. These low field dipoles are located at about 200 m and at 430 m upstream and downstream IPA providing a bending angle of 135 μrad each. The aim of our study was to determine SR photons coming from these dipoles and entering the TAS that might impact the detector, also possibly crossing the Beryllium beam pipe from -8 m to 8 m around IPA. Figure 26 shows a zoom of this region.

As reference position we have chosen the TAS. We give the power of the photons passing through the TAS and look in detail where these photons were generated and calculate the energy spectra and hit positions downstream of the TAS and determine the fraction of photons hitting the inner Beryllium pipe.

Table 4 gives the exact longitudinal position of the last eight dipoles 470 m upstream the IPA. The critical energy in the dipoles is 0.536 keV, the mean energy 0.165 keV and the emitted power by each dipole is 6.4 W. In total, their power emitted is about 50 W. However, only a fraction of these photons will reach the experimental area, due to geometrical reasons and to the TAS presence, and even fewer of them will hit the ±8 m Beryllium beam pipe.

As described above we used MDISim to produce the geometry and the magnetic field description. GEANT4 has been used to perform the detailed simulation, starting at approximately -700 m from IPA with a Gaussian beam with the expected size and emittance. These protons were tracked with the Monte Carlo, taking into account the production of SR photons and their subsequent propagation. For this study the baseline and ultimate optics were used, with and without the horizontal crossing angle. The results of this simulation, summarized in Table 5, suggest that about 10 W are expected to enter the experiment area with no crossing angle. The power of the photon flux at the inner Beryllium pipe located from -8 m to 8 m around IPA remains below 1 W. A possible 10 Tm detector spectrometer placed in the experimental area would increase this value by one Watt. Even if the power deposited on the Beryllium pipe
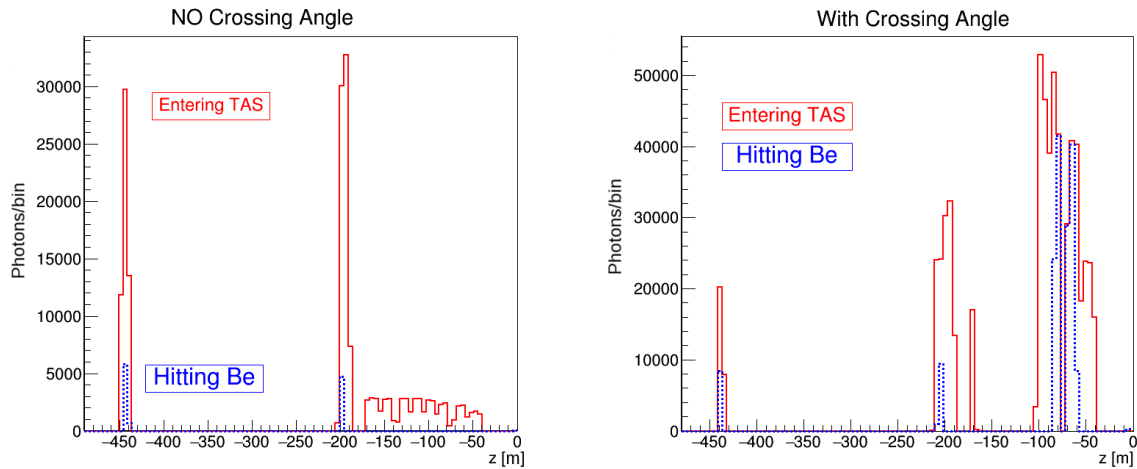
Figure 27: Histogram of SR photon generation upstream IPA for the ultimate optics, where IPA is at z=0. **Left plot:** *The two peaks at -450 and -200 m are photons produced by 2 T dipoles that reach the two TAS regions (in red), but few of them hit the Be pipe (in blue). In addition, few photons at are generated by quadrupole magnets downstream -200 m, and none of them hit the Be beam pipe.* **Right plot:** *With crossing angle, additional radiation comes from quadrupole magnets in the last 100 m. Radiation coming from MQXD.A2LA.H at -77.6 m and MQXC.B1LA.H at -56.3 m hits the Be pipe.*

remains small, the simulations show that the number of photons is significant and merits a closer investigation. To evaluate the amount of particles that can pass through the Beryllium, we also used a more local GEANT4 simulation, in which the photons with the energy spectra obtained from the beams were directly impacting at a 200 μrad grazing angle on the 0.8 mm Beryllium pipe, to provide an upper limit estimate for the ultimate crossing angle.

Table 5 summarizes the study of the SR impacting the experimental area. Without crossing angle, the SR emitted by beam protons in the last magnetic elements upstream IPA is small and only a very minor source of backgrounds to the experiments. With crossing angle, we get a small increase in power and a more significant increase in the number of photons reaching the experimental area. A small part of the increase is due to the extra SR generated by the field of the corrector magnets that generate the crossing angle (shown in Table 6). We find that the power from the SR of the corrector magnets is 0.6 W for the baseline and 1.8 W for the ultimate lattices, or a rather small increase compared to the power produced by the 11.3 m long 2 T dipoles. Figure 27 shows the z-position at the origin of the photons reaching the TAS. We can see, that without crossing angle (left plot of Figure 27), almost all photons entering the experimental originate in the 2 T dipoles located -450 and -200 m upstream of IPA, and that only few of these hit the Beryllium beam pipe. The simulation includes SR from quadrupoles which increases significantly with crossing angle over the last 100 m as can be seen in Figure 27). With crossing angles many of these photons and in particular those generated by the quadrupole magnets MQXD.A2LA.H at -77.6 m and MQXC.B1LA.H at -56.3 m will hit the Beryllium pipe. The magnetic field gradient of these quadrupoles in the last 100 m does not vary much between the different optics configurations. Much of the increase with crossing angle is from the last

quadrupoles.
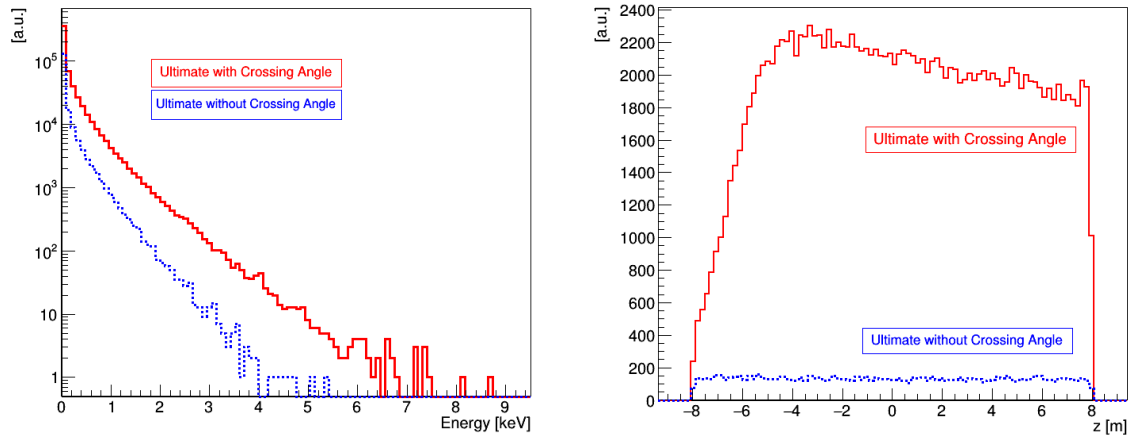
Figure 28: **Left:** *Photon energy distribution entering the TAS with crossing angle (in red), and without crossing angle (in blue) for the ultimate optics.* **Right:** *Photons hitting point in the last -8 m to 8 m Be beam pipe around IPA located at z=0. Without crossing angle (in blue) the photons are uniformly distributed, while With crossing angle (in red) they accumulate towards the center.*

In conclusion, the contribution of SR photons into the experimental area has been addressed by means of a detailed GEANT4 simulation using MDISim. Similar studies were also carried out for other lattice versions [45] and the results have been benchmarked with SYNRAD [46], finding a very good agreement.

The results presented here show that the synchrotron radiation backgrounds are not expected to be an issue for the experimental areas.

Table 4: Longitudinal position of the the last eight dipoles 470 m upstream the IPA. They are all 2 T and 11.3 m, their critical energy is 0.536 KeV, mean energy is 0.165 keV and each has an the emitted power of 6.4 W. In total the emitted power is about 50 W.

Dipole name	Distance from IPA [m]
MBXW.A4LA.H	190.0
MBXW.B4LA.H	202.8
MBXW.C4LA.H	215.6
MBXW.D4LA.H	228.4
MBRW.A4LA.H1	421.3
MBRW.B4LA.H1	434.1
MBRW.C4LA.H1	446.9
MBRW.D4LA.H1	459.7

Table 5: Summary of the SR power emitted per beam in the last 700 m upstream IPA that reaches the experimental area P_{TAS}, and the fraction that impacts the inner Be beam pipe P_{Be}, for the baseline and ultimate configurations with and without crossing angle. The number of photons hitting the Be $N_{\gamma Be}$ and their mean energy E_{mBe} are also shown.

Lattice	Version	Half Crossing Angle [μrad]	P_{TAS} [W]	P_{Be} [W]	$N_{\gamma Be}$ [10^9]	E_{mBe} [keV]
Baseline	LATTICE_V9	0	8.5	0.74	1.1	0.166
Ultimate	LATTICE_V9	0	8.7	0.73	1.1	0.163
Baseline	LATTICE_V9	52	26.5	1.17	1.8	0.163
Ultimate	LATTICE_V9	100	46.4	12.86	16.0	0.198

Table 6: Correctors upstream IPA used in the optics lattices with crossing angle.

Corrector name	Distance to IPA [m]	Length [m]	B field [T]	
			Baseline	Ultimate
MCBXDHV.A2LA.H	75.8	1.3	-0.168	-0.562
MCBXCHV.3LA.H	174.2	1.3	1.226	1.957
MCBRDH.4LA.H1	474.0	3.0	-0.821	-1.536

Table 7: Properties of quadrupole groups in alternative triplet.

Parameter	Quadrupole		
	Q1	Q2	Q3
Sub-Magnets	2	3	2
Sub-Magnet Length [m]	15	15	15
Coil Radius [mm]	96.5	96.5	96.5
Gradient [T/m]	106	112	99
Shielding [mm]	44.2	33.2	24.2

6   ALTERNATIVE TRIPLET AND FLAT OPTICS

In parallel to the final focus triplet described in Section 3.1, efforts were made to design an alternative triplet [47]. This alternative was designed using an algorithm that systematically scans the design parameter space to find the shortest possible triplet that has sufficient beam stay clear and shielding [48]. In a first approximation, the code scans through the entire design parameter space to estimate the beam stay clear using the thin lens approximation. It then does a more precise scan using the MAD-X aperture module in a smaller area identified by the approximation.

The design was worked in iteratively with energy deposition studies to determine the right amount of shielding required to protect the triplet from the collision debris. In a first iteration, the optimisation code was used to find the shortest triplet with 1.5 cm of tungsten shielding. This triplet was integrated into the baseline EIR and energy deposition studies were performed to estimate the amount of shielding needed. Next, the triplet was optimised again with the new shielding estimate and again integrated and tested. This process was repeated several times until a triplet was found that is as short as possible whilst still having sufficient beam stay clear and shielding.

In the course of this optimisation it was found that peaks in energy deposition could be minimized if all triplet quadrupoles had similar coil radii [49, 50]. Therefore, the optimisation code was modified to find triplets made of quadrupoles of equal radii. In order to fulfill the technical requirements, the quadrupoles of the ideal solution had to be split into sub-magnets that were no longer than 15 m. The resulting triplet consisted of seven 15 m sub-magnets with equal radii and similar gradients – the details of the magnets in this triplet are shown in Table 7. Like the baseline triplet, the main quadrupoles in the alternative triplet are separated by 7 m drifts to leave space for correctors and instrumentation, whilst the sub-magnets only need 2 m separation to leave room for connectors.

The triplet was integrated into the same EIR as in Section 3.1, leaving the same 18.8 m drift between Q3 and the first separation dipole for the correction package. The matching quadrupoles in the EIR were used to match the Twiss functions to the arc. The resulting optics in the triplet are shown in Fig. 29, which also shows the beam orbit for a 100 μrad crossing in the horizontal plane.

Once the triplet was integrated the beam stay clear in the individual quadrupoles was reassessed and the shielding was increased wherever possible. This lead to an increase in shielding in Q2 and Q1 by 9 mm and 20 mm respectively. These increases are possible because the β functions and orbit are smaller near the front of the triplet, hence leaving more space for poten-
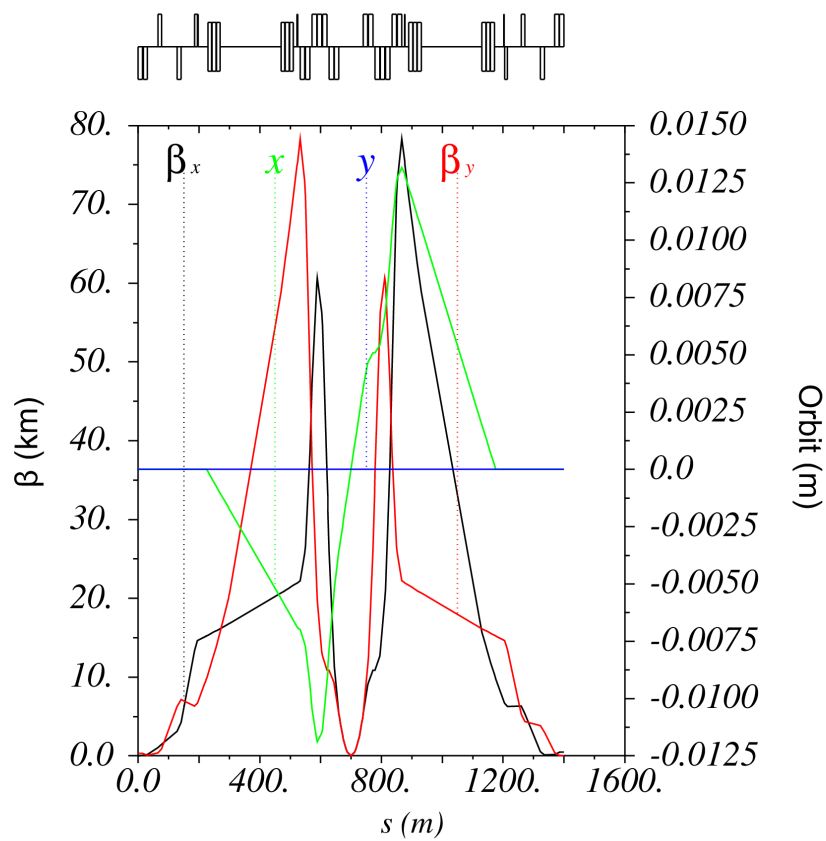
Figure 29: β functions and orbit for EIR optics with alternative triplet and $\beta^*_{x,y} = 0.3$ m.
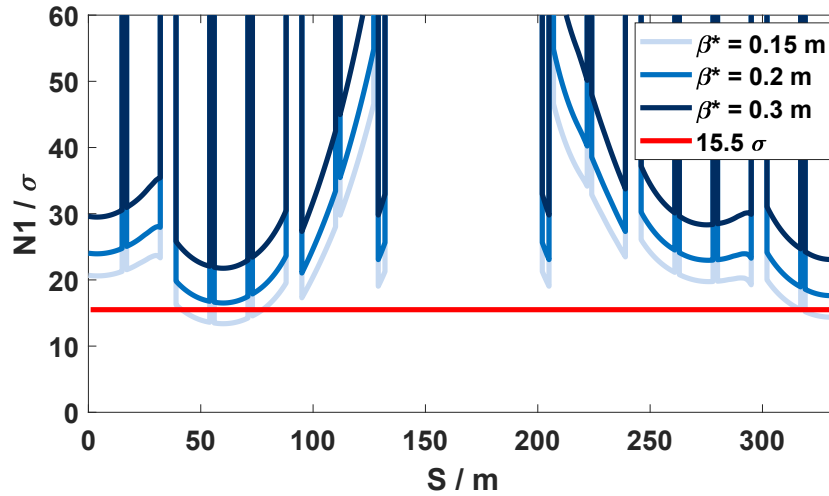
Figure 30: Plot showing BSC for $\beta^* = 0.15$ m, 0.2 m and 0.3 m for the alternative triplet.

tial shielding. This distribution in shielding is advantageous since most of the collision debris will hit the magnets closer to the IP. The exact amounts of shielding are also shown in Table 7.

Whilst the ultimate collision optics aims for a $\beta^*_{x,y}$ of 0.3 m, the shielding was designed to leave 15.5σ for an optics with a $\beta^*_{x,y}$ of 0.2 m to provide a luminosity handle. The aperture studies were performed using the same technical specifications for the cooling, cold bore and beam screen as outlined in Section 3.1 and the results are shown in Fig. 30. As one can see from Fig. 30, the alternative triplet can comfortably reach a β^* of 0.3 m and even 0.2 m. Figure 30 also shows the beam stay clear for a case with $\beta^* = 0.15$ m, whilst this is lower than the required it may still be a viable option should the beam current be low enough to change the collimator settings accordingly. A low beam current may be one of the reasons why the β^* would need to be decreased in the first place to compensate for the loss in luminosity.

The alternative triplet can also be used for a flat optics, which can be exploited to compensate for the luminosity loss in case of any problem with the crab cavities [49]. This can be achieved without changing the gradients in the triplet but re-matching the β functions using the matching section quadrupoles. It was decided that a 1.2 m × 0.15 m flat optics would provide sufficient luminosity. Table 8 shows a comparison between the main parameters of the round and flat optics. The corresponding crossing angle for the flat optics had to be increased by 30 %, and the same increase for the beam-beam separation, that moved from 17 σ to 22 σ. The reason comes from beam-beam studies, that suggest increasing the crossing angle by 43 % for a flat beam factor of 4 [51].

Table 8: Parameters of the different optics for the alternative triplet.

Parameter	Round	Flat
β^*_x [m]	0.3	1.2
β^*_y [m]	0.3	0.15
Full crossing angle [μrad]	200	130
Beam-beam separation [σ]	17	22
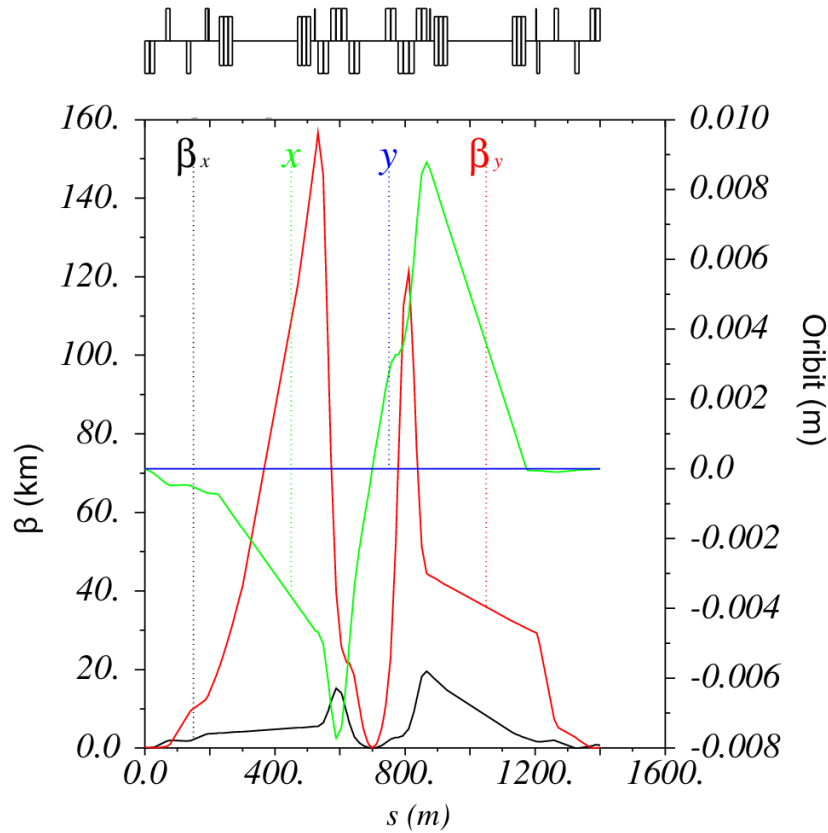
Figure 31: β Functions and orbit for 1.2×0.15m flat EIR collision optics with alternative triplet and $\beta_x^* =1.2$ m, $\beta_y^* =0.15$ m.
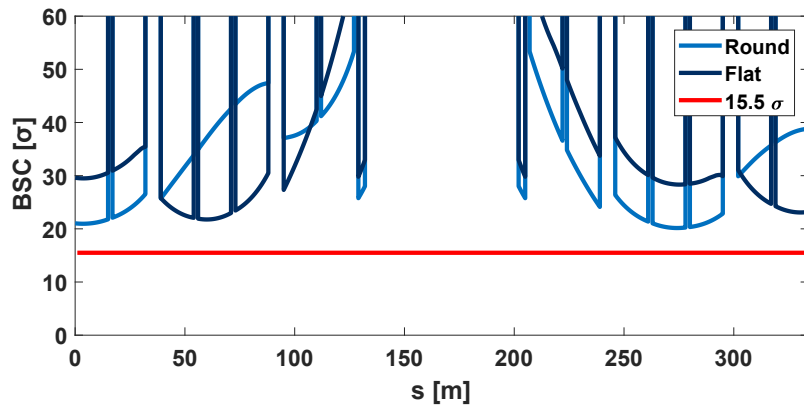
Figure 32: Plot showing BSC in triplet for flat and round optics.

Figure 31 shows the EIR optics for the flat option. The corresponding BSC are shown in Fig. 32. The flat optics still provides sufficient BSC.

6.1 ENERGY DEPOSITION IN ALTERNATIVE TRIPLET
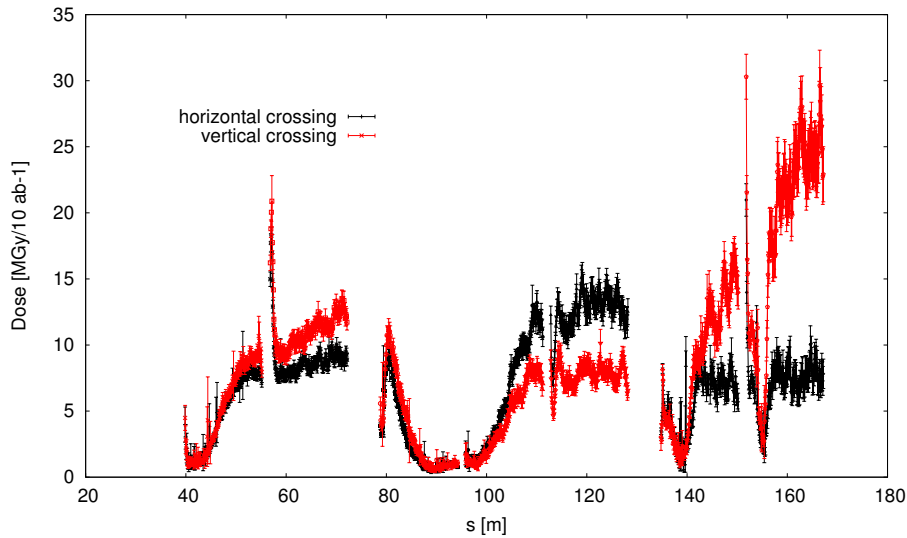
Figure 33: Peak dose profile for alternative triplet (round optics).
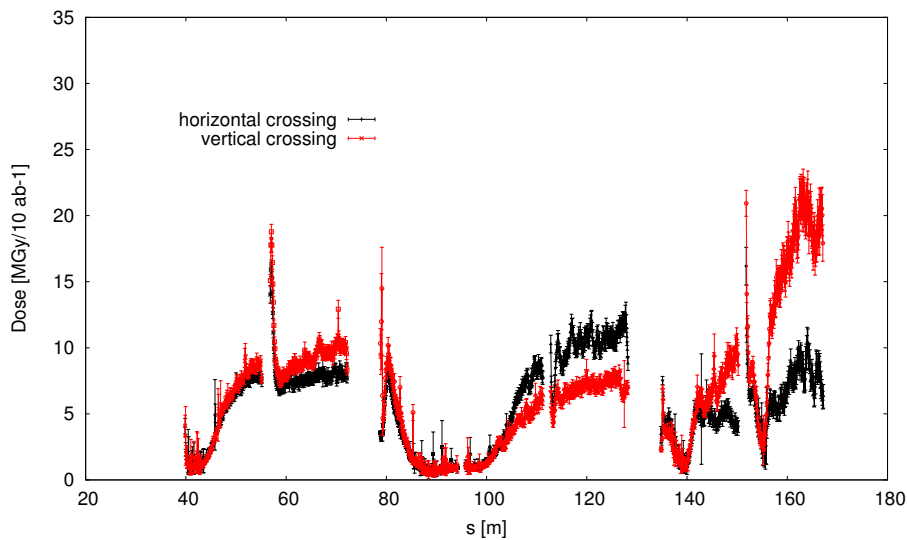
Figure 34: Peak dose profile for the alternative triplet (flat optics).

Figure 33 shows the peak dose in the triplet magnets along the longitudinal axis. The maximum dose is found at Q3, with a maximum of 30 MGy/10 ab^{-1} (excluding the peak at the beginning, that can be reduced by reducing the missing gap for the interconnects). This means 65 MGy for the entire life of the magnet, assumed to resist, at least, an integrated luminosity of 18.5 ab^{-1}. The dose can also be reduced when using the alternate crossing scheme, in a similar ways as the baseline triplet [1, 36]. On the other hand, the peak dose profile for the alternative flat beam option is shown in Fig. 34. The peak dose is reduced to from 55 to 42 MGy for 18.5 ab^{-1}, due to the lower crossing angle allowed by the flat beam optics.

7 LOW LUMINOSITY EIRS

In addition to the high luminosity IRs, located in Point A and G, the FCC-hh will also host two low luminosity experimental insertions in Point B and L. Similar to the LHC, in these insertion also the beams from the injector chain will be injected upstream of the experiments. Due to initial injection hardware considerations, the length of half cells containing such hardware has been set to 150 m. Contrary to the LHC injection/experimental insertions, two additional half cells were added after the injection cells. These give the possibility to add more injection protection elements to protect both the superconducting magnets and experiment from mis-injected beam. Due to this, the interaction point is not located in the center of the straight section but rather 250 m further downstream. Unlike the high luminosity experimental insertions, currently no required performance is established for these low luminosity experiments and subsequently no target β^* can be specified. Similarly, due to the lack of a detector design and required cavern length, the L^* has been tentatively set to 25 m. The layout of this combined injection/experimental insertion for Point B based on these considerations is presented in Fig. 35.
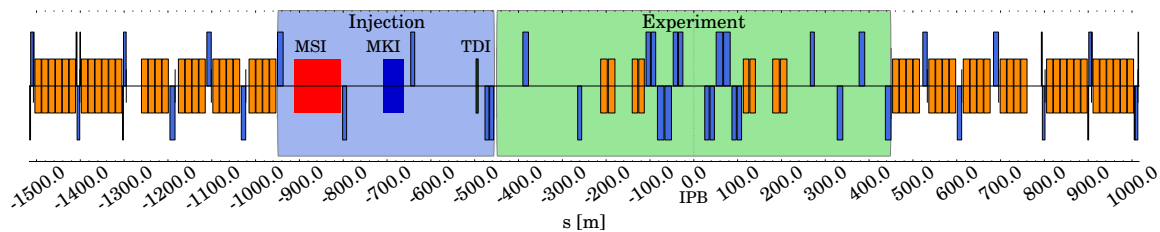
Figure 35: Layout of the low luminosity insertion in Point B.

The final focus triplet left and right of the interaction point consists of three quadrupoles. Each one of these quadrupoles is split into two submagnets to keep the magnet length below 15 m. Each one of the Q1 and Q3 submagnets has a length of 10 m wheres each Q2 submagnet is 15 m long. Between each submagnet, a drift space with a length of 2 m has been reserved for the interconnects. All triplet quadrupoles have the same coil aperture of 64 mm. The specifications of the triplet quadrupole can be found in Tab. 20. This aperture is further reduced, because of the presence inside the coil of a liquid helium layer, a Kapton insulator layer, and the stainless steel cold bore, as described in Sec. 3.1. A 10 mm thick tungsten (INERMET180) shielding is finally put inside the cold bore to mitigate the radiation in the superconducting coils. The available radial aperture for the beam is therefore reduced to 18.25 mm. In order to keep the separation section after the triplet as short as possible a superconducting solution was chosen. Using two 12.5 m long shared aperture separation dipoles D1 with a field strength of 12 T and two 15 m long double aperture recombination dipoles D2 with a field strength of 10 T the length of this section can be keep under 100 m. Due to the aforementioned considerations on the injection hardware and the added additional cells the matching sections in these insertions feature a different length and layout. On the non-injection side of the insertion, four matching quadrupoles make up the matching section which is 235 m long. The 735 m long matching section on the injection side of the insertion consist six matching quadrupoles. Between Q8 and Q9 the injection septum (MSI) is located which deflects the injected beam in the vertical plane. In the following half cell between Q7 and Q8 the injection kicker system (MKI) is installed which provides a horizontal kick to put the injected beam on the closed orbit. The quadrupole Q8 between the MSI and the

MKI was chosen to be horizontally defocussing to provide an additional horizontal kick which helps in reducing the required kick strength of the injection kickers. A 4 m long absorber (TDI) to protect superconducting magnets further downstream from misinjected beam is installed in the cell between Q6 and Q7. Each of these half cells is 150 m long.

Both the optics for collision energy as well as for an injection energy are presented in Fig. 36. At collision energy a minimum β^* of 3 m has been matched. The crossing angle for these insertion
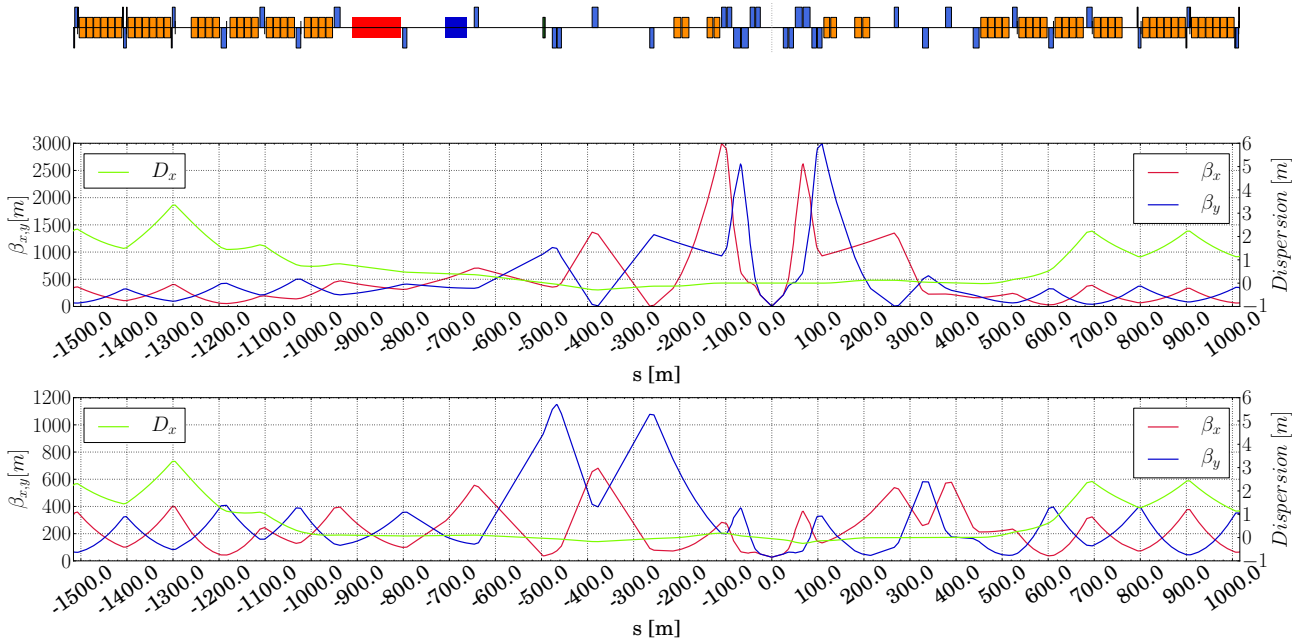
Figure 36: *Collision optics (top) and injection optics (bottom) for the low luminosity insertion in Point B.*

has obtained from scaling the normalized separation of the high luminosity insertion [52] with the reduced number of long range encounters. This leads to a normalized separation of 5.25σ, corresponding to a half crossing angle of 19.5 µrad. With this crossing angle the beam stay clear in the triplet is well above the minimum allowed beam stay clear of 15.5 σ and could be further increased, which is illustrated in Fig. 37. However, a crossing angle giving the requested beam separation of 30 σ at full intensity would lead to a beam stay clear below limit of 15.5 σ. To comply with both constraints, the β^* at begin of collision then has to be set to 19 m. The minimum β^* of 3 m could then be reached after 1.5 hours, assuming a reduction of the separation to 20 σ at this point. During collision, the beams are always colliding with transverse offset to keep the beam-beam tune shift below 1-2 $\times 10^{-3}$.

At injection energy, the crossing angle is limited by the triplet aperture to a beam separation of 7 σ. Further studies are required to assess the viability of this separation. If the separation proves to be insufficient, the shielding in the triplet could be reduced, in turn potentially decreasing also the achievable integrated luminosity.

For the injection optics various constraints had to be taken into account to provide optimum injection protection efficiency. The horizontal phase advance between the MKI and the TDI should be 90° to ensure any kicker failure translating into an orbit offset at the TDI. The beta functions at the TDI were matched to the largest possible values to increase the beam size which
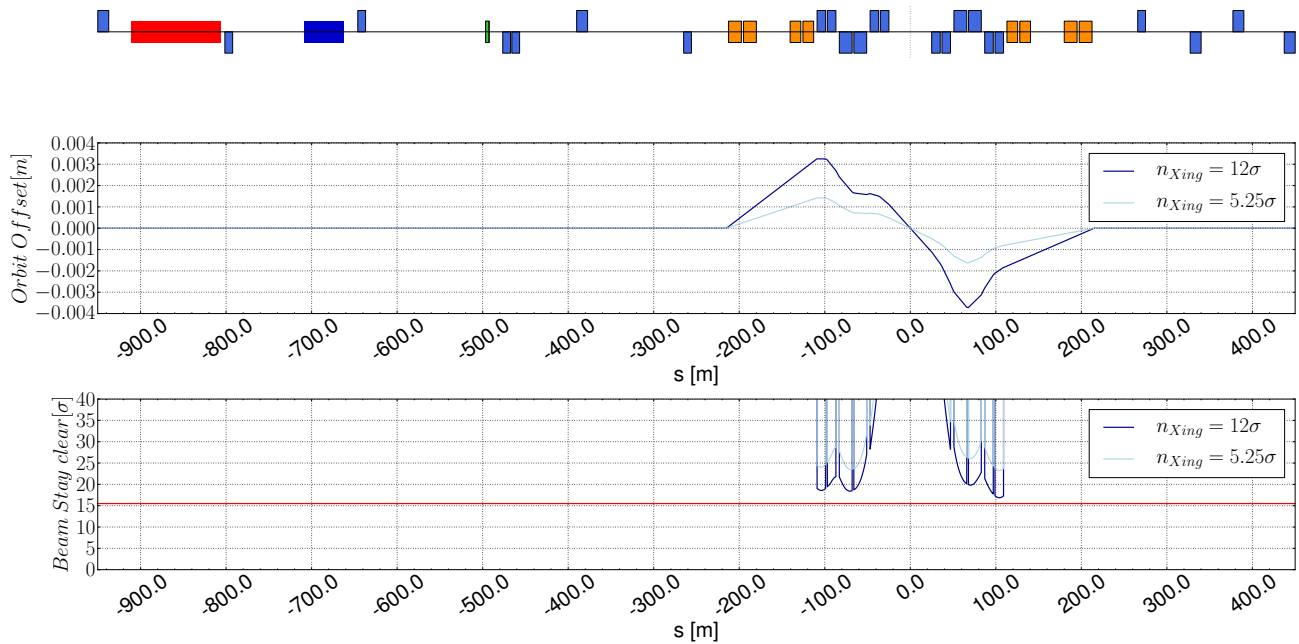
Figure 37: Crossing angle and corresponding aperture in the low luminosity insertion in Point B. The minimum allowed beam stay clear of 15.5 σ is indicated in red.

in turn reduces the peak energy density in case of an injection kicker malfunction. Furthermore, the dispersion function in the straight section is kept below 30 cm.

As the injection of beam 2 will take place in Point L the low luminosity insertion for this straight section is mirrored with respect to s. Here the interaction point is located 250 m upstream of the middle of the straight section for beam 1. Both the collision optics with a β^* of 3 m and injection optics with a β^* of 27 m are illustrated in Fig. 38.

7.1 ENERGY DEPOSITION IN THE LOW LUMINOSITY EIR

The energy deposition in the low luminosity EIR has been assessed with FLUKA simulations, for both vertical and horizontal crossing.

For this purpose, the insertion region has been modelled, as shown in Fig. 39. The quadrupole design is very similar to the one for the main EIR described in Section 3.1, but the model has been scaled down to cope with the smaller coil radius of 32 mm. In order to better protect the superconducting magnets, the 10 mm thick tungsten shielding is prolonged in the interconnect cold bore, with tentative gaps of 70 cm. In addition to this, a mask has been put in front of the Q1A, to shield its entrance. The mask is clearly visible in Fig. 39 and it is modelled as a 76 cm long tungsten (INERMET180) cylinder with an external radius of 81 mm and a free radial aperture of 13.26 mm.

The power impacting on each magnet is reported in Table 9 for the shielding and the cold mass separately, assuming an instantaneous luminosity of 5×10^{33} cm^{-2} s^{-1}. Even if the mask in front of Q1A intercepts about 280 W, this magnet remains the most exposed and the total power on the cold mass is about 150 W for both crossing schemes.

Less than 40% of the total power generated in the collision is deposited in the inner triplet.
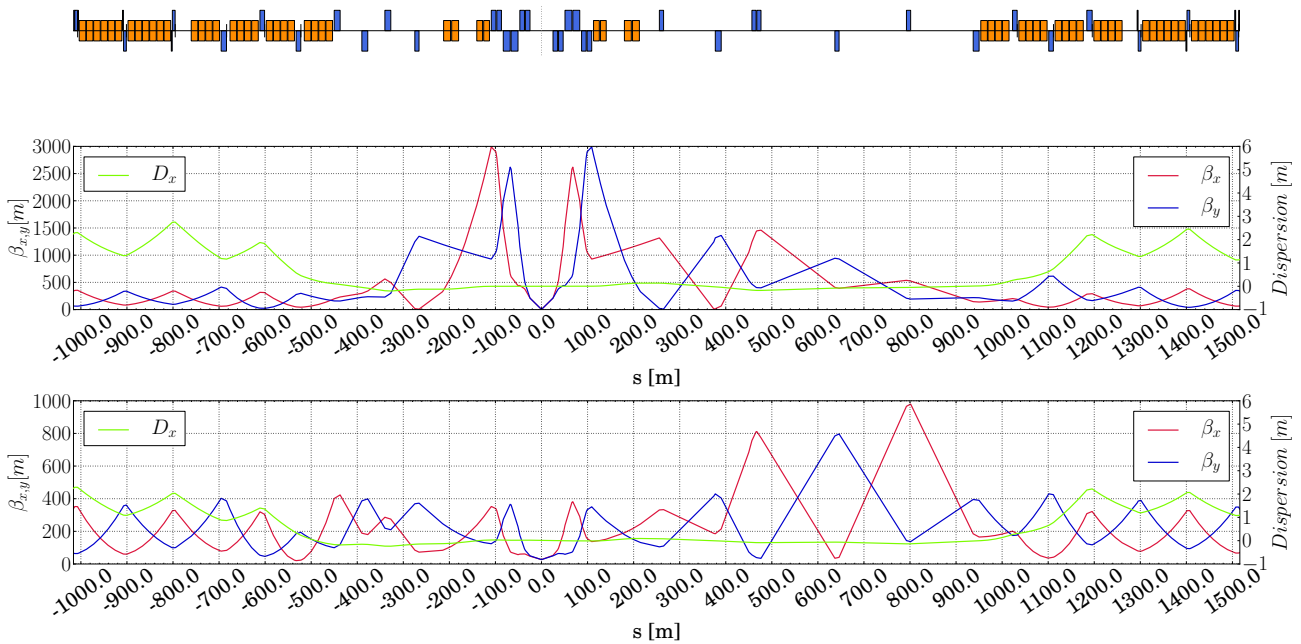
Figure 38: Collision optics (top) and injection optics (bottom) for the low luminosity insertion in Point L.
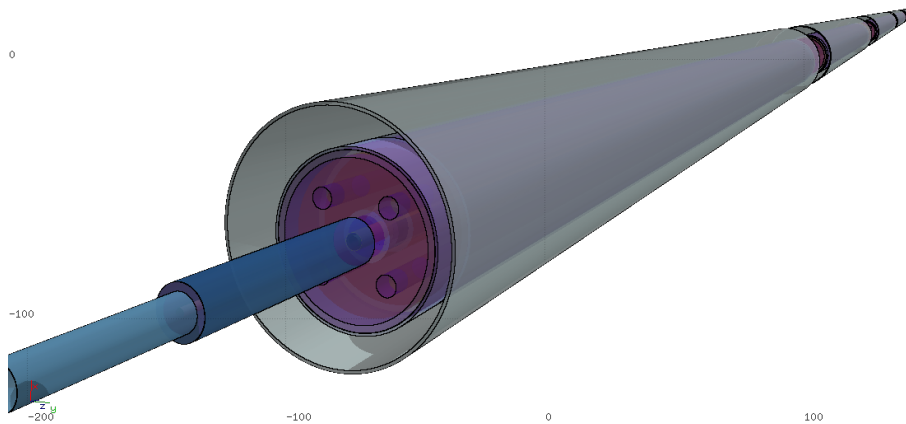
Figure 39: Low luminosity triplet geometry as modelled in FLUKA.

The remaining 63%, which corresponds to about 2.7 kW for an instantaneous luminosity of 5×10^{33} cm^{-2} s^{-1}, escapes downstream on both sides of the IP and it will be deposited elsewhere in the accelerator.

Figure 40 shows the spectra of particles at the exit of Q3B for vertical crossing on the left and horizontal crossing on the right. The peak at 50 TeV is due to protons produced in single diffractive events. These protons travel much further in the accelerator and are expected to impact in the Dispersion Suppression region. The charged pions and the protons of few tens of TeV will instead be lost on D1, on the TAN or in the matching section. Many high energy photons and neutrons escape as well downstream Q3 and they will be captured by the TAN or even at longer distances from the IP, depending on on their angle. In order to precisely assess

Table 9: *Total power in the magnets of the inner triplet for vertical and horizontal crossing, assuming an instantaneous luminosity of 5×10^{33} cm^{-2} s^{-1}. The contribution to the shielding and the cold mass are quoted separately.*

Magnet	Vertical Crossing [W]			Horizontal Crossing [W]		
	Total	Shielding	Cold Mass	Total	Shielding	Cold Mass
Q1A	249	101	147.9	251	102	149
Q1B	268	183	85	269	184	85
C1	27	19	8	28	19	8
Q2A	118	82	36	119	83	36
Q2B	204	147	57	191	137	54
Q3A	111	77	34	113	80	33
Q3B	113	81	31	132	95	37
C2	15	11	4	18	13	5
Total	**1105**	**701**	**404**	**1121**	**714**	**407**
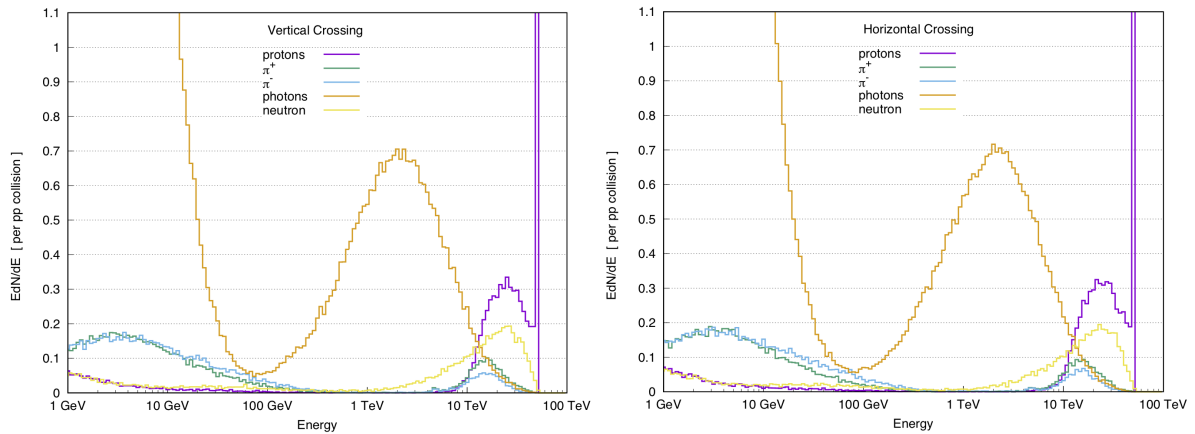
Figure 40: *Spectra of collision debris particles in the vacuum chamber at the exit of Q3B for vertical crossing (left) and horizontal crossing (right) schemes. The distributions are normalised to one proton-proton collision.*

the impact of these particles in the accelerator components, new calculations are foreseen, which will extend the simulation to the matching section, as it has been done for the main interaction region.
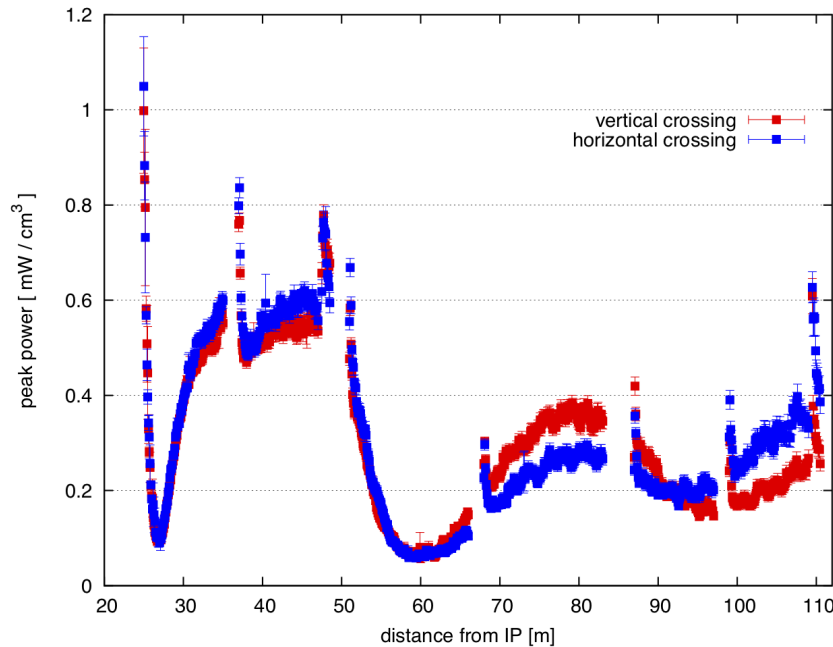
Figure 41: Peak power density in the innermost cable of the inner triplet magnets as a function of the distance from the IP, for an instantaneous luminosity of $5 \ 10^{33} \ cm^{-2} \ s^{-1}$. The resolution along the z-axis is 10 cm and the resolution on the azimuthal direction is 2 deg. A radial average is considered along the cable thickness (18.6 mm for quadrupoles and 5 mm for correctors) and the maximum over the azimuthal direction is considered.

The peak power density in the magnet inner cable is presented in Figure 41 as a function of the distance from the interaction point for both the vertical and the horizontal crossing. For both cases, the values are safely below the quench limit for the superconducting coils. The maximum is indeed 1 mWcm^{-3} and it is reached at the entrance of Q1A. Without the presence of the mask, this value would be more than 30 times higher and would significantly exceed quench limits. The presence of a peak at the entrance of each magnet is due to the shielding gaps in the interconnects.

For what concerns the dose, the maximum is reached as well at the entrance of Q1A for both schemes and, for an integrated luminosity of 500 fb^{-1}, it remains below 30 MGy, which is the limit presently assumed for the damage of insulators and organic materials.

The cause of the shape difference between the red and the blue curves in Fig. 41 is the different crossing scheme of the collisions. The crossing choice influences as well the azimuthal position of the peaks. This can be seen from Fig. 42, which shows the dose distribution in the innermost strands of the magnet coils as a function of the distance from the IP and of the azimuthal angle Φ, for vertical crossing on top and horizontal crossing on bottom. The observed asymmetric pattern is due to the combined effects of the crossing angle and plane and of the focusing/defocusing action of the quadrupoles, which sweep low energy secondary particles into the magnets, preferentially along the vertical and horizontal planes.
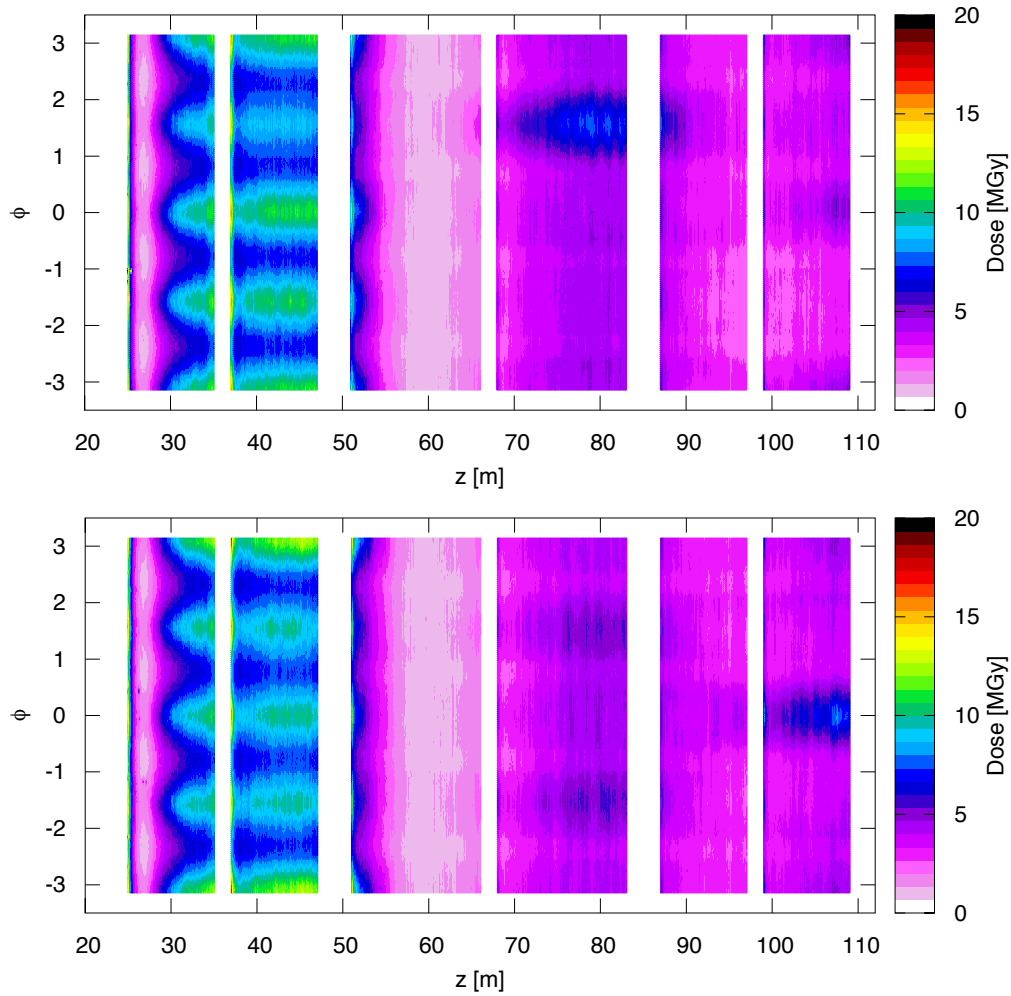
Figure 42: Dose distribution averaged over the innermost 3 mm of the magnet coils, as a function of z and of the azimuthal angle for vertical (top) and horizontal (bottom) crossing, normalised to an integrated luminosity of $500\,\mathrm{fb}^{-1}$.

The triplet polarity is DFD in the horizontal plane for positive particles, which are more abundant in p-p collisions. In Q1 positive particles are therefore deflected in the horizontal plane and, in the case of vertical crossing, hit the coil symmetrically at 0 and π. On the vertical plane, negative particles impact at $-\frac{\pi}{2}$[1], because of the crossing angle offset. In the case of horizontal crossing, positive particles impact mainly at π, because of the initial crossing angle. For this reason both peak power density and peak dose values in Q1A and Q1B are higher for this case. The lower peaks at $\pm\frac{\pi}{2}$ are due to negative particles symmetrically deflected in the vertical plane. Due to the polarity change in Q2, positive particles are deflected on the vertical plane and impact at $\frac{\pi}{2}$ for the vertical case, because of the initial crossing angle. In the case of h-crossing two symmetric and lower peaks are present at $\pm\frac{\pi}{2}$. Finally in Q3, where the polarity is inverted again, positive particles are deflected in the horizontal plane and are collected at 0 for h-crossing, while for v-crossing they hit symmetrically at 0 and at π. Higher power density and dose values are therefore observed in Q3B for the horizontal crossing.

---

[1]The position of the peak is $-\frac{\pi}{2}$, because the crossing angle is negative. In the case of positive crossing, the peak would have been at $\frac{\pi}{2}$.

8 CROSS TALK BETWEEN EXPERIMENTAL INSERTION REGIONS

Proton collisions at the interaction points of the FCC-hh may contribute to background in the subsequent detector, and losses between the detectors. As the proton luminosity is high, this may be of concern.

Using the upgraded version of the DPMJET-III event generator [53] inside FLUKA [32] we generate the debris from the 50 TeV proton-proton (pp) collisions with vertical crossing. Due to the rigidity of the charged particles, only protons are transported by the accelerator. Muons are the only other major concern, and are treated separately. The energy distribution of protons is large, this is shown in Fig. 43.
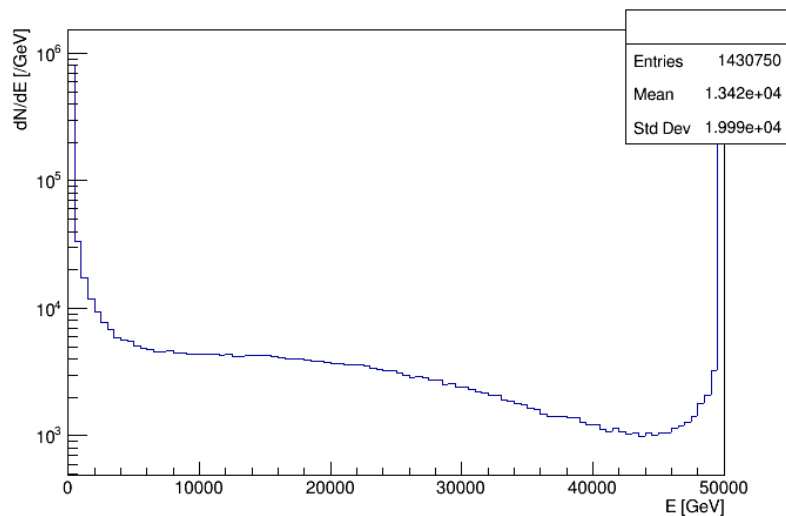
Figure 43: Proton energy distribution 3 m downstream of IPA for 10^6 pp collision events.

For proton cross-talk, we use the energy of 49.95 TeV as a threshold. Protons from the collision with energy greater than this are defined as 'elastic', and those with energy below this are defined as 'inelastic' protons. PTC [54] and MERLIN [55] are used to perform tracking of both elastic and inelastic protons to determine the cross-talk. That is, the number of collision debris protons that will reach the next detector. We generate the debris at IPA and track to IPB.

For the case of elastic protons, nearly all reach IPB with a spot size similar to that of the beam. This is likely to lead to an emittance growth, but should pose no major concern. Around 2 inelastic protons per bunch crossing will arrive at IPB under nominal settings, this rises to $\approx$ 9 under ultimate settings. The mean energy of these few protons is 49.89 TeV, and they are unlikely to be of concern in terms of cross-talk.

What is of greater concern is the loss of inelastic protons between the two IPs. Most are lost in the short straight section and dispersion suppressor (DS) regions post IPA. The losses per element, found using PTC tracking, are shown in the top plot of Fig. 44. In these simulations all apertures are treated as black absorbers. A detailed study of losses in the detector, inner triplet, and separation and recombination dipoles has been conducted in detail with FLUKA. This is documented in section 4. Therefore we focus on losses after these elements, of which, the DS losses are of great concern as they are bottlenecks for off-momentum particles and the proton energy is high.

It was decided to mitigate these losses using HL-LHC style 'TCLD' collimators in the DS. Two 1 m long TCLD collimators were placed before the first quadrupole in cells 8 and 10, at the points where the dispersion rises rapidly. With these collimators in place, the DS losses are minimised, as shown in the lower plot in Fig. 44.
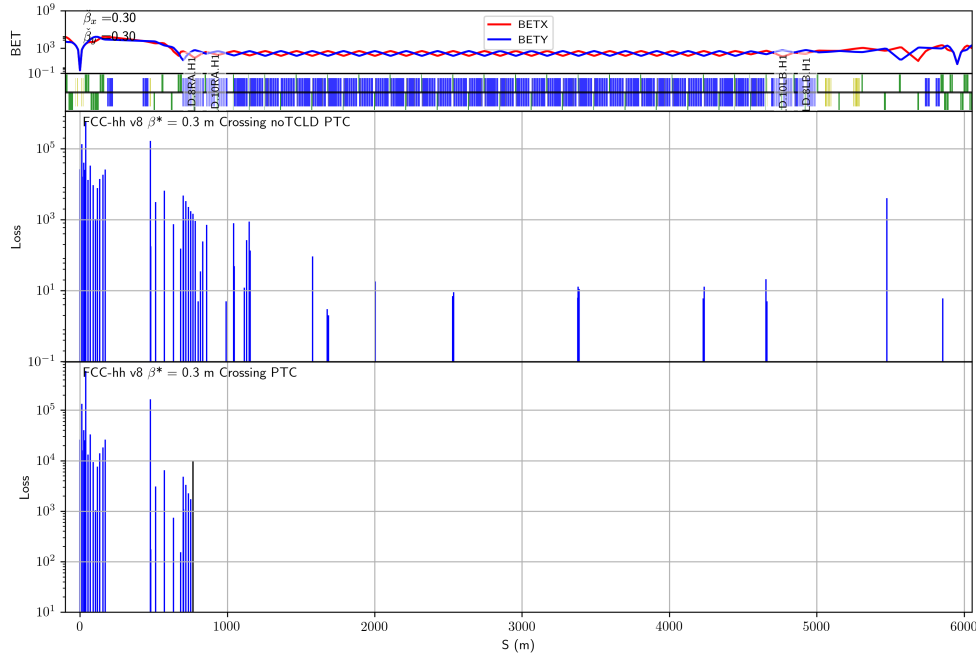
Figure 44: Proton losses between IPA and IPB per element. The top loss map does not include any collimators, the bottom loss map includes two TCLD style collimators in front of the first quadrupole in cells 8 and 10.

These collimators are placed in regions of relatively low β function, thus allowing larger jaw gaps so as not to violate the collimation hierarchy. A jaw half-gap of 35 σ was found to be sufficient. Using MERLIN the power and energy of lost particles in the short straight section are shown, in the presence of the two TCLD collimators, in Fig. 45. We note that all losses are shown per element, therefore the largest peak in the power plot corresponds to the loss over the full length of a $\approx$ 200 m long drift.

Collimators clean the 'primary' halo, but produce a 'secondary' halo in turn. In order to verify that this secondary shower would not exceed the maximum energy deposition allowed on the subsequent superconducting quadrupole, a two step simulation was used. Firstly the inelastic protons were transported from IPA to the TCLDs using MERLIN, to generate hits on the collimator jaws. These hits were fed into a FLUKA model, shown in Fig. 46, which consists of the first TCLD collimator, a drift space, followed by a 50 cm long mask prior to the superconducting quadrupole. The quadrupole coils are simulated as a mixture of 50% niobium-3-tin and 50% copper. Inermet180 has been chosen as the material for the TCLD jaw and quadrupole mask, as in the current LHC absorbers. The distance between the collimator and
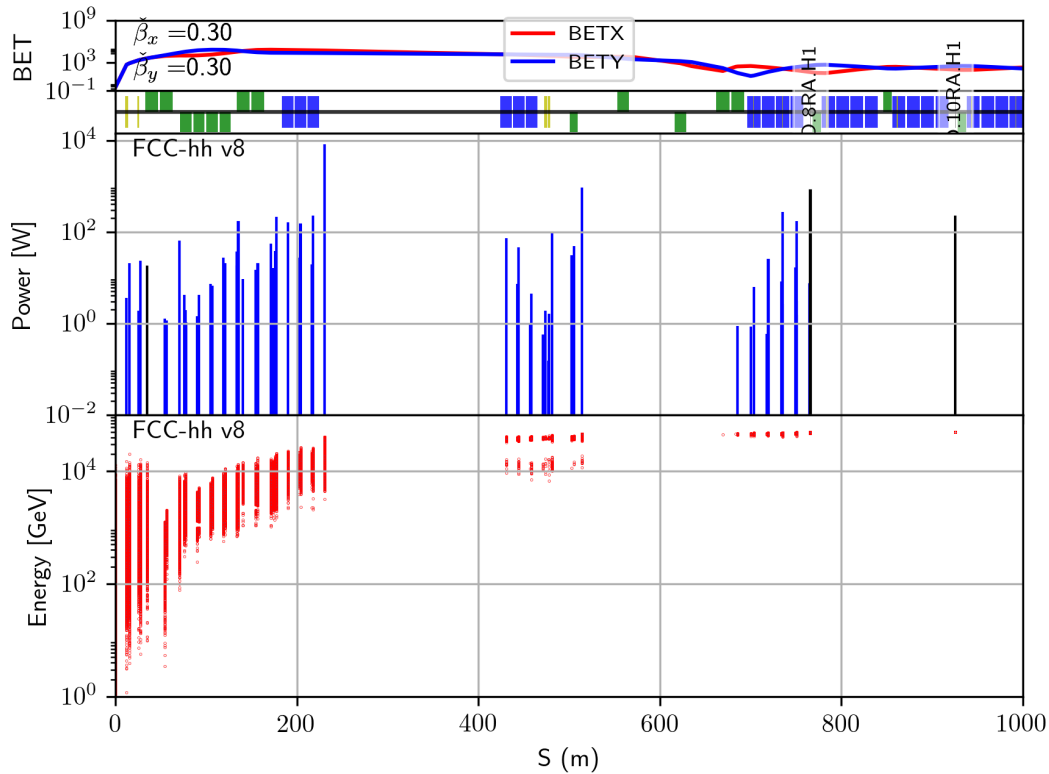
Figure 45:   Proton losses between IPA and IPB. The top plot shows power deposition per element when including the TCLD collimators, the bottom plot shows the energy distribution of the losses.

the mask and quadrupole gives space for the shower to spread, thus minimising the load on the quadrupole coils.

As the first collimator (in cell 8) has the higher load, it was used for shower simulations. A jaw half-gap of 35 σ was shown to intercept all inelastic protons whilst not violating the betatron collimation hierarchy. There is the possibility that this could still interfere with the momentum cleaning hierarchy - as the momentum cleaning was not defined at the time of this investigation.

It is evident from Fig. 47, which shows the maximum energy deposition in the first quadrupole post-TCLD, that the 50 cm mask is required in order to stay below the limit of $\approx$ 5 - 10 mW cm^3 [56] at ultimate parameters. For baseline parameters the mask is not required. Thus we may mitigate the DS losses due to inelastic protons from collision debris using the two 1 m long Inermet180 TCLDs, placed in cells 8 and 10, before the first quadrupole in the cell.

As muons have a large mean free path, they can travel kilometres in dense materials, therefore muon cross-talk may be a concern. The muon energy distribution generated from 10^6 50 TeV pp collisions using DPMJET-III inside FLUKA is shown in Fig. 48. The highest energy muon produced is around 20 TeV.

We may separate muon energy loss into; ionisation, bremsstrahlung, production of electron-positron pairs, and through photo-nuclear and photo-nucleon interactions. This approach is
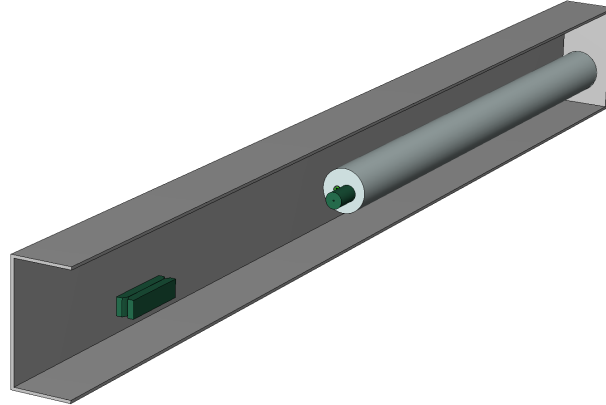
Figure 46: *FLUKA model used for shower simulations in the dispersion suppressor. The green objects are first the TCLD collimator, followed by a 50 cm long mask, both made of Inermet180. Following this is the first quadrupole in the DS. The particles are loaded 63 cm before the collimator.*
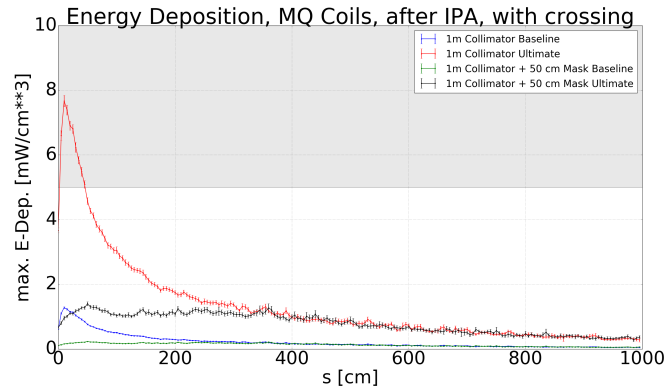
Figure 47: *Maximum energy deposition per cm^3 in 5 cm bins along the first quadrupole in cell 8 after IPA for baseline and ultimate configurations.*

summarised in equation 3 [57]:

$$\left\langle \frac{-dE}{dx} \right\rangle = a(E) + b(E)E, \tag{3}$$

where $a(E)$ is the ionisation contribution, and $b(E) = b_b(E) + b_p(E) + b_n(E)$ is the sum of the contributions of bremsstrahlung, pair production, and photo-nuclear/nucleon interactions [58]. In the continuous slowing down approximation the range is given by

$$R(E) = \int_{E_0}^{E} (a(E') + b(E')E')^{-1} dE'. \tag{4}$$

At high energy a and b are constant, and this becomes
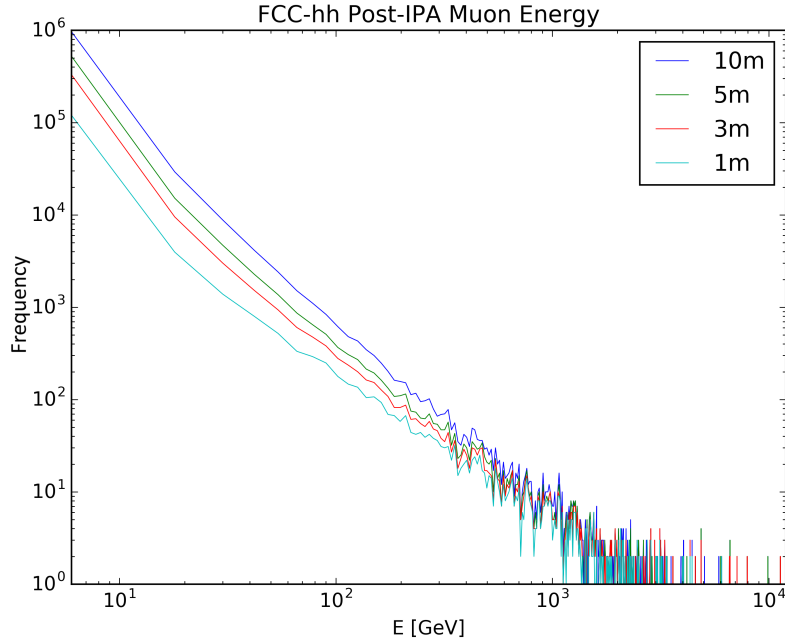
Figure 48: Muon energy distribution at intervals downstream of IPA, generated using DPMJET-III in FLUKA, with no detector or accelerator model.

$$R(E) \approx \frac{1}{b} ln \left(1 + \frac{E}{E_c} \right), \tag{5}$$

where the electronic and radiative losses are equal at the critical energy E_c. We use this approach to calculate the theoretical range of muons in standard rock, which has a specific gravity of $2.65\,\mathrm{g\,cm^{-3}}$ and $\left\langle \frac{Z}{A} \right\rangle = 0.5$, and in which the muon critical energy is 693 GeV. The result of this calculation is shown in Fig. 49, which gives a maximum range of 3.3 km for collision debris muons in the FCC-hh through standard rock. This analytical calculation does not include the interaction of collision debris with the detector.
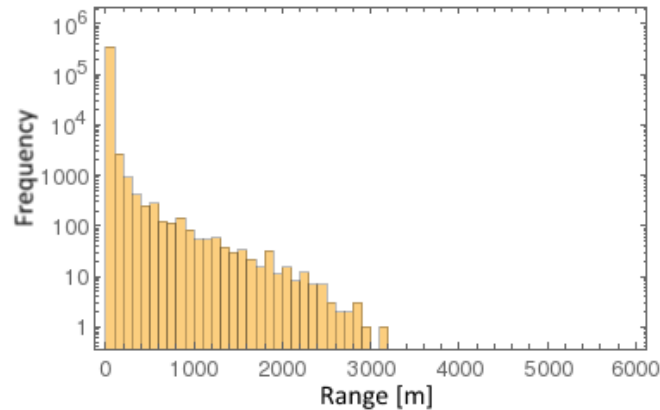
Figure 49: Theoretical range of collision debris muons in rock.

In order to verify the analytical expectation, 5×10^4 *pp* collisions were generated using DPMJET-III inside FLUKA with a complete model of the detector [59] in order to generate

the initial muon distribution. These muons were then tracked in FLUKA using a total of 10^9 histories through the tunnel model shown in Fig. 50.
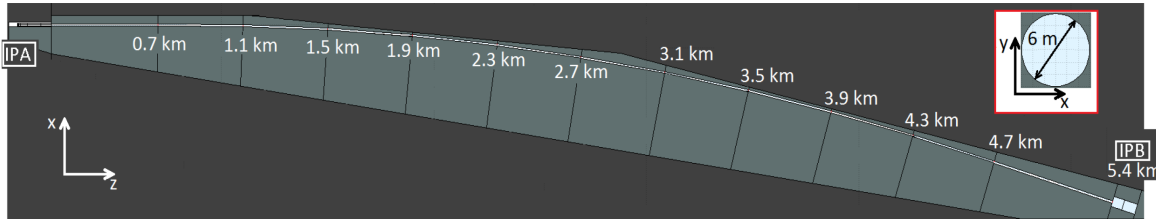
Figure 50: Cross secton of the FLUKA FCC-hh tunnel model. The distance from IPA to each point along the tunnel central line is indicated. IPB is located 5.4 km away from IPA. The lighter grey area is modelled as standard rock. Note that this model was based on an older version of the FCC-hh lattice.

The muon energy distributions along the tunnel model are shown in Fig. 51. From this it is clear that no muons travel beyond 2.7 km, thus we may conclude that muon cross-talk should not be an issue at the FCC-hh.
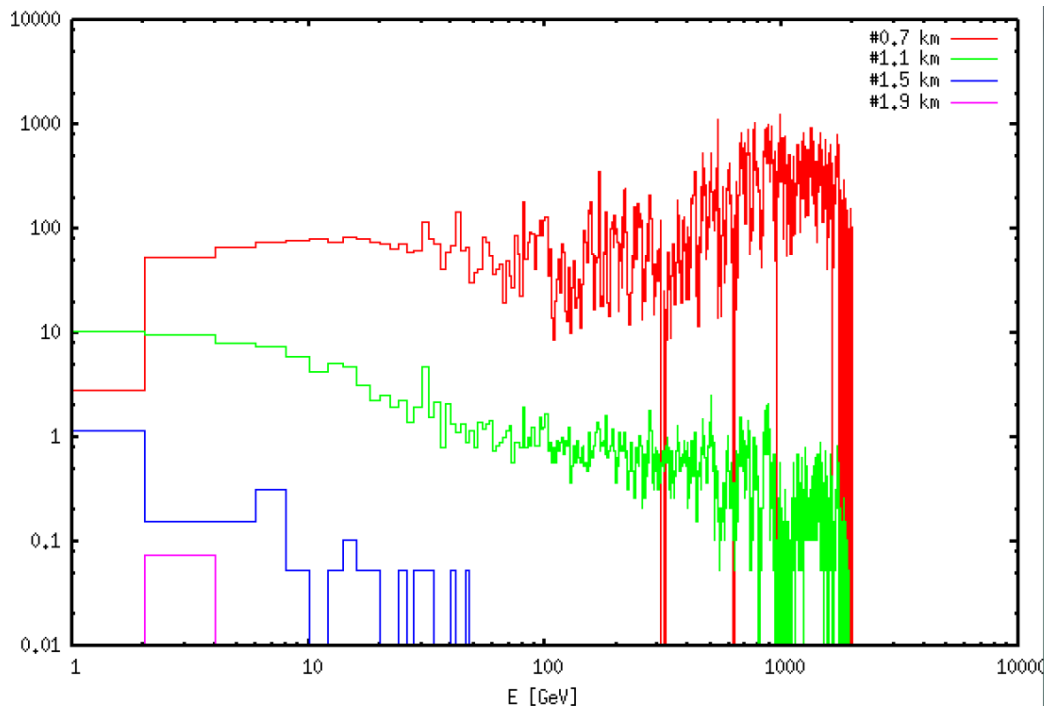
Figure 51: Muon distribution at different positions along the tunnel.

In summary, elastic protons with an energy greater than 49.95 TeV from collisions at IPA nearly all reach IPB with a spot size similar to the beam. This should result in an emittance growth of the beam. Inelastic protons, with an energy less than 49.95 TeV pose a greater threat. Only 2 - 9 inelastic protons per bunch crossing are foreseen to reach IPB, this is deemed negligible. The losses from inelastic protons in the short straight section and dispersion suppressor regions post IPA are of concern. By using two 1 m long TCLD collimators with Inermet180 jaws, the

Table 10: Parameters of triplet of the high luminosity EIRs.

Magnet	Coil aperture diameter [mm]	Gradient [T/m]	Length [m]	Number per IP
Q1	164	130	14.3	4
Q2	210	105	12.5	8
Q3	210	105	12.5	4

losses in the DS region post IPA was mitigated. Shower simulations of the inelastic proton impacts upon the first TCLD in cell 8 were performed in order to gauge secondary shower damage on the next superconducting element, the first quadrupole in the cell. Results show that for baseline parameters the energy deposition is below the suggested limit, and for the ultimate parameters the addition of a 50 cm long Inermet180 mask would be required to protect the quadrupole coils [60].

Despite high energy muons of up to 20 TeV being created in the *pp* collisions, by analytical and Monte Carlo methods we have shown that muons should not travel far enough through rock or the accelerator tunnel to reach the subsequent detector [61].

Photons and other charged hadrons in the collision debris are ignored as their rigidity means that they will not be accepted in the accelerator, and thus cannot be transported to IPB.

9   HARDWARE SPECIFICATIONS

Table 10 lists the specification for the triplet quadrupoles of the high luminosity EIRs. The cryostats of the triplet quadrupoles will have to be designed so they can support thick and consequently heavy shielding inside the coil apertures. The field quality specifications used in dynamic aperture studies are shown in Tables 11 and 12.

For the separation and recombination dipoles D1 and D2 in the high luminosity EIRs, normal conducting dipoles, similar to the MBXW and MBW designs of the LHC, were chosen because of the radiative environment and because they can provide better field quality. The hardware need are listed in Table 13 and the assumed field qualities in Tables 14 and 15.

The parameters of the matching section quadrupoles of the high luminosity EIRs are shown in Table 16.

The required strengths of the non-linear corrector package behind the triplet were obtained from the dynamic aperture studies. The coil apertures are the same as in the triplet quadrupoles Q2 and Q3 in order to avoid exposure to collision debris. With this the possible field strengths could be determined [62] and the lengths requirements calculated. The results are listed in Table 17. The sextupole and octupole correctors are require only lengths of a few centimetres. Thus it is possible to increase the coil apertures of the sextupole and octupole correctors further in order to reduce energy deposition if necessary.

Table 18 lists the hardware specifications of the high luminosity IR orbit correctors. The single aperture MCBX magnets have nested coils, allowing them to deflect the beam in both planes. Each matching section quadrupole is equipped with one orbit corrector of the same aperture, hence the need for 3 classes. The MCB class is identical to the arc orbit correctors and

Table 11: *Field error components of Q1 and Q3 with $R_{ref} = 55\,\text{mm}$ for Q1 and $R_{ref} = 70\,\text{mm}$ for Q3.*

Normal	Systematic		Uncertainty		Random	
	Injection	High Field	Injection	High Field	Injection	High Field
b_1	0.000	0.000	0.000	0.000	0.000	0.000
b_2	0.000	0.000	0.000	0.000	(10)	(10)
b_3	0.000	0.000	0.82	0.82	0.82	0.82
b_4	0.000	0.000	0.57	0.57	0.57	0.57
b_5	0.000	0.000	0.42	0.42	0.42	0.42
b_6	-19.947	-0.357	1.1	1.1	1.1	1.1
b_7	0.000	0.000	0.19	0.19	0.19	0.19
b_8	0.000	0.000	0.13	0.13	0.13	0.13
b_9	0.000	0.000	0.07	0.07	0.07	0.07
b_{10}	3.664	-0.129	0.2	0.2	0.2	0.2
b_{11}	0.000	0.000	0.26	0.26	0.26	0.26
b_{12}	0.000	0.000	0.18	0.18	0.18	0.18
b_{13}	0.000	0.000	0.009	0.009	0.009	0.009
b_{14}	0.158	-0.866	0.023	0.023	0.023	0.023
b_{15}	0.000	0.000	0.000	0.000	0.000	0.000
Skew						
a_1	0.000	0.000	0.000	0.000	0.000	0.000
a_2	-0.877	-0.877	0.000	0.000	(10)	(10)
a_3	0.000	0.000	0.65	0.65	0.65	0.65
a_4	0.000	0.000	0.65	0.65	0.65	0.65
a_5	0.000	0.000	0.43	0.43	0.43	0.43
a_6	0.062	0.062	0.31	0.31	0.31	0.31
a_7	0.000	0.000	0.19	0.19	0.19	0.19
a_8	0.000	0.000	0.11	0.11	0.11	0.11
a_9	0.000	0.000	0.08	0.08	0.08	0.08
a_{10}	0.002	0.002	0.04	0.04	0.04	0.04
a_{11}	0.000	0.000	0.026	0.026	0.026	0.026
a_{12}	0.000	0.000	0.014	0.014	0.014	0.014
a_{13}	0.000	0.000	0.01	0.01	0.01	0.01
a_{14}	-0.004	-0.004	0.005	0.005	0.005	0.005
a_{15}	0.000	0.000	0.000	0.000	0.000	0.000

Table 12: *Field error components of Q2 with $R_{ref} = 70$ mm.*

Normal	Systematic		Uncertainty		Random	
	Injection	High Field	Injection	High Field	Injection	High Field
b_1	0.000	0.000	0.000	0.000	0.000	0.000
b_2	0.000	0.000	0.000	0.000	(10)	(10)
b_3	0.000	0.000	0.82	0.82	0.82	0.82
b_4	0.000	0.000	0.57	0.57	0.57	0.57
b_5	0.000	0.000	0.42	0.42	0.42	0.42
b_6	-19.752	-0.317	1.1	1.1	1.1	1.1
b_7	0.000	0.000	0.19	0.19	0.19	0.19
b_8	0.000	0.000	0.13	0.13	0.13	0.13
b_9	0.000	0.000	0.07	0.07	0.07	0.07
b_{10}	3.631	-0.132	0.2	0.2	0.2	0.2
b_{11}	0.000	0.000	0.26	0.26	0.26	0.26
b_{12}	0.000	0.000	0.18	0.18	0.18	0.18
b_{13}	0.000	0.000	0.009	0.009	0.009	0.009
b_{14}	0.151	-0.865	0.023	0.023	0.023	0.023
b_{15}	0.000	0.000	0.000	0.000	0.000	0.000
Skew						
a_1	0.000	0.000	0.000	0.000	0.000	0.000
a_2	-1.003	-1.003	0.000	0.000	(10)	(10)
a_3	0.000	0.000	0.65	0.65	0.65	0.65
a_4	0.000	0.000	0.65	0.65	0.65	0.65
a_5	0.000	0.000	0.43	0.43	0.43	0.43
a_6	0.071	0.071	0.31	0.31	0.31	0.31
a_7	0.000	0.000	0.19	0.19	0.19	0.19
a_8	0.000	0.000	0.11	0.11	0.11	0.11
a_9	0.000	0.000	0.08	0.08	0.08	0.08
a_{10}	0.002	0.002	0.04	0.04	0.04	0.04
a_{11}	0.000	0.000	0.026	0.026	0.026	0.026
a_{12}	0.000	0.000	0.014	0.014	0.014	0.014
a_{13}	0.000	0.000	0.01	0.01	0.01	0.01
a_{14}	-0.007	-0.007	0.005	0.005	0.005	0.005
a_{15}	0.000	0.000	0.000	0.000	0.000	0.000

Table 13: *Parameters of separation and recombination dipoles of the high luminosity EIRs.*

Magnet	Length [m]	Field strength [T]	Coil aperture diameter [mm]	Number per IP
D1	11.3	2	170	8
D2	11.3	2	91	8

Table 14: *Field error components of D1 with $R_{ref} = 46$ mm. The values are based on the MBXW magnet design for LHC.*

Normal	Systematic		Uncertainty		Random	
	Injection	High Field	Injection	High Field	Injection	High Field
b_1	0.000	0.000	0.000	0.000	0.000	0.000
b_2	-0.200	-0.300	0.000	0.000	0.100	0.200
b_3	0.100	-0.900	0.000	0.000	0.300	0.000
b_4	0.000	0.000	0.000	0.000	0.000	0.000
b_5	-0.100	-0.100	0.000	0.000	0.200	0.000
Skew						
a_1	0.000	0.000	0.000	0.000	0.000	0.000
a_2	-0.200	-0.100	0.000	0.000	0.200	0.100
a_3	0.000	0.000	0.000	0.000	0.000	0.100
a_4	0.000	0.000	0.000	0.000	0.000	0.000
a_5	0.000	0.000	0.000	0.000	0.000	0.100

Table 15: *Field error components of D2 with $R_{ref} = 28$ mm. The values are based on the MBW magnet design for LHC.*

Normal	Systematic		Uncertainty		Random	
	Injection	High Field	Injection	High Field	Injection	High Field
b_1	0.000	0.000	0.000	0.000	0.000	0.000
b_2	0.300	-1.400	0.000	0.000	1.800	1.100
b_3	1.500	-0.400	0.000	0.000	0.400	0.800
b_4	0.000	0.300	0.000	0.000	0.400	0.800
b_5	-0.400	-0.500	0.000	0.000	0.300	0.200
b_6	0.000	0.000	0.000	0.000	0.400	0.300
b_7	-0.300	-0.200	0.000	0.000	0.200	0.200
b_8	0.000	0.100	0.000	0.000	0.200	0.200
b_9	-0.100	0.000	0.000	0.000	0.000	0.200
b_{10}	0.000	0.100	0.000	0.000	0.000	0.200
b_{11}	0.000	0.100	0.000	0.000	0.000	0.100
Skew						
a_1	0.000	0.000	0.000	0.000	0.000	0.000
a_2	0.100	0.200	0.000	0.000	0.100	0.200
a_3	0.000	-0.100	0.000	0.000	0.100	0.300
a_4	0.000	0.100	0.000	0.000	0.000	0.200
a_5	0.000	-0.100	0.000	0.000	0.000	0.100
a_6	0.000	0.000	0.000	0.000	0.100	0.200
a_7	0.000	-0.100	0.000	0.000	0.000	0.100
a_8	0.000	0.000	0.000	0.000	0.000	0.100

Table 16: Parameters of matching quadrupoles of the high luminosity EIRs.

Magnet	Length [m]	Field strength [T/m]	Coil aperture diameter [mm]	Number per IP
Q4	9.1	200	70	2
Q5/6	12.8	260	60	4
Q7	14.3	400	50	4

Table 17: Specifications of the non-linear correctors.

Magnet	Coil aperture diameter [mm]	Field strength	Length [m]
Sextupole (normal/skew)	210	$460\,\mathrm{T/m^2}$	0.07
Octupole (normal/skew)	210	$4000\,\mathrm{T/m^3}$	0.21

two units are placed next to Q7 in order to provide enough strength. No strengths requirements for the low luminosity EIR orbit correctors have been established so far, but we expect to require 4 single aperture correctors per IP in the triplet region, as well as 5 double aperture correctors with 70 mm coil aperture per IP and 5 double aperture correctors with 50 mm coil aperture per IP.

Orbit correction studies have shown that the alignment tolerances for the high luminosity EIR elements listed in Table 19 result in a residual orbit below 1 mm (90th percentile). It should be noted that the residual orbit is very sensitive to misalignments of the strong Q7 quadrupoles. Thus those elements need to be aligned more precisely than the other matching quadrupoles, possibly requiring a remote alignment system as proposed for the HL-LHC [63].

For collision optics beyond ultimate parameters (with β^* down to 0.2 m) a crab voltage of 18.1 MV per beam on either side of each high luminosity IP was sufficient to provide full crabbing. This corresponds to 145 MV in total. Following a direct scaling from the HL-LHC lattice, 20 m of space were allocated for the crab cavities on each side of the two main IPs. No detailed studies on number of cavities or cryostat design were done yet. It should be noted that a radiation mitigation strategy to protect the triplet is to change the crossing plane on the two main IPs at least once during the lifetime. This will also require an exchange of the crab cavities (horizontally/vertically deflecting). Since IPA and IPG will always run with different

Table 18: Specifications of the high luminosity IR orbit correctors.

Magnet	Coil aperture diameter [mm]	Field strength [T]	Length [m]	Number per IP
MCBX	210	3	1.3	6
MCBRD	70	4	3.0	4
MCBYM	60	4	1.5	4
MCB	50	4	1.2	4

Table 19: Alignment specifications for the high luminosity EIR elements.

Element	Error	Units	Value	Comments
Separation dipole D1	roll angle $\sigma(\phi)$	mrad	1.0	
Recombination dipole D2	roll angle $\sigma(\phi)$	mrad	1.0	
Triplet quadrupoles Q1-Q3	$\sigma(x), \sigma(y)$	mm	0.2	
Matching quadrupoles Q4-Q6	$\sigma(x), \sigma(y)$	mm	0.5	
Matching quadrupole Q7	$\sigma(x), \sigma(y)$	mm	0.2	remote alignment
BPM	$\sigma(x), \sigma(y)$	mm	0.3	
	$\sigma(\text{read})$	mm	0.05	accuracy

Table 20: Parameters of triplet of the low luminosity EIRs.

Magnet	Coil aperture diameter [mm]	Gradient [T/m]	Length [m]	Number per IP
Q1	64	270	10	4
Q2	64	270	15	4
Q3	64	270	10	4

crossing planes, it should be possible to simply exchange the hardware between the two main IPs during a shutdown. This should be taken into account when designing the cryostats and RF connections.

The specifications for the triplet quadrupoles in the low luminosity experimental insertions are listed in Table 20.

Contrary to the high luminosity EIRs, the separation and recombination dipoles in the low luminosity EIRs are chosen to be superconducting. This allows a significantly shorter separation, providing more space for both experiment and the injection hardware.

The specifications for the two types of quadrupoles used in the matching section of these insertion are presented in Table 22.

10 BEAM OPTICS AND LATTICE FILES

A repository of FCC-hh can be found at http://fccr.web.cern.ch/FCCr/hh/FCC-hh-lattice/. It contains the lattice version this report is based on. The high luminosity EIR lattice, together

Table 21: Parameters of the separation and recombination dipoles in the low luminosity EIRs.

Magnet	Coil aperture diameter [mm]	Field strength [T]	Length [m]	Number per IP
D1	100	12	12.5	4
D2	60	10	15	4

Table 22: Parameters of matching quadrupoles in the low luminosity EIRs.

Magnet	Coil aperture diameter [mm]	Gradient [T/m]	Length [m]	Number per IP
Type Short	70	200	9.1	6
Type Long	50	300	12.8	5

with aperture files and optics settings can be found in the `exp_section/` directory. The file `job.sample.madx` can be run by MAD-X to load the sequence and generate a Twiss and Survey file as well as calculate the apertures. The low luminosity EIR lattices are located in the `low_lumi_exp_inj_section/` directory. Similarly, an example `job.sample.madx` can be run to obtain the optics function and lattice geometry.

The folder `Collider/` contains the fully integrated ring. Files with names of the form `fcc_hh_####.madx` and `fcc_hh_####_cross.madx` are the main MAD-X files loading all necessary parts with or without crossing angles enabled. Here `####` denotes the β^* in the high luminosity IRs in mm.

The magnet field quality assumptions used in the tracking studies so far can be found in the files `errors/MQX_errortable_v2`, `errors/D1_errortable_v0` and `errors/D2_errortable_v0` for the final focus quadrupoles, the separation dipoles and the recombination dipoles respectively.

11 REFERENCES

[1] R. Martin, M. I. Besana, F. Cerutti, A. Langner, R. Tomás, E. Cruz-Alaniz, and B. Dalena, "Interaction region design driven by energy deposition," *Phys. Rev. Accel. Beams*, vol. 20, p. 081005, Aug 2017.

[2] "Future Circular Collider Study. Volume 3: The Hadron Collider (FCC-hh) Conceptual Design Report." preprint edited by M. Benedikt et al. CERN accelerator reports, CERN-ACC-2018-0058, December 2018. Submitted to Eur. Phys. J. ST.

[3] E. Cruz-Alaniz, D. Newton, R. Tomás, and M. Korostelev, "Design of the large hadron electron collider interaction region," *Phys. Rev. Accel. Beams*, vol. 18, p. 111001, Nov 2015.

[4] R. de Maria, "Layout design for final focus systems and applications for the LHC interaction region upgrade," Tech. Rep. LHC-PROJECT-Report-1051. CERN-LHC-PROJECT-Report-1051, 2007. revised version submitted on 2007-12-13 16:58:30.

[5] A. Louzguiti, "Electromagnetic design of the fcc lattice (ms) and corrector (mcs) sextupoles and lattice octupoles (mo)." Presentation at the FCC week 2018, Amsterdam, the Netherlands, https://indico.cern.ch/event/656491/contributions/2938717/attachments/1628570/2594643/FCC_Sextupoles_and_Octupoles_design_AL_anim.pdf.

[6] J. B. García *et al.*, "Beam-beam studies for FCC-hh." FCC week 2018, Amsterdam, April, 2018,.

[7] W. Herr, X. Buffat, R. Calaga, R. Giachino, G. Papotti, T. Pieloni, and D. Kaltchev, "Long Range Beam-beam Effects in the LHC," in *Proceedings, ICFA Mini-Workshop on Beam-Beam Effects in Hadron Colliders (BB2013): CERN, Geneva, Switzerland, March 18-22 2013*, pp. 87–92, 2014.

[8] T. Pieloni *et al.*, "Two Beam Effects," in *Proc. 2014 Evian Workshop on LHC Beam Operation*, (Geneva), pp. 69–79, CERN, CERN, 2014.

[9] X. Buffat, G. Arduini, E. Bravin, G. Iadarola, E. Metral, Y. Papaphilippou, D. Pellegrini, S. Redaelli, B. Salvachua, M. Solfarloli, G. Trad, D. Valuch, J. Wenninger, J. Barranco, T. Pieloni, C. Tambasco, and M. Crouch, "Long-range and head-on beam-beam: what are the limits?," in *7th Evian workshop on LHC beam operation: Evian-les-Bains, France.*, (Geneva), pp. 133–140, CERN, CERN, 2017.

[10] T. Pieloni, *A study of beam-beam effects in hadron colliders with a large number of bunches*. PhD thesis, Ecole Polytechnique Federale de Lausanne (EPFL), 2008.

[11] W. Herr, "Features and implications of different LHC crossing schemes," Tech. Rep. LHC-Project-Report-628. CERN-LHC-Project-Report-628, CERN, Geneva, Feb 2003.

[12] http://sixtrack.web.cern.ch/SixTrack/, 2016.

[13] F. Schmidt, "Sixtrack User's Reference Manual," tech. rep., CERN, 1994.

[14] W. Herr and T. Pieloni. `http://lhc-beam-beam.web.cern.ch/lhc-beam-beam/combi_welcome.html`.

[15] T. Pieloni and W. Herr, "Coherent beam-beam in the CERN large hadron collider (LHC) for multiple bunches, different collision schemes and machine symmetries," in *Proceedings of 2005 Particle Accelerator Conference*, 2005.

[16] T. Pieloni and W. Herr, "Models to study multi bunch coupling through head-on and long-range beam-beam interactions," cern lhc project report 937 and proceedings of EPAC06, edinburgh, united kindom, 2006, CERN, 2006.

[17] M. Crouch, *Luminosity Performance Limitations due to the Beam-Beam Interaction in the Large Hadron Collider*. PhD thesis, Manchester University, 2017.

[18] M. Giovannozzi, "Proposed scaling law for intensity evolution in hadron storage rings based on dynamic aperture variation with time," *Phys. Rev. ST Accel. Beams*, vol. 15, p. 024001, Feb 2012.

[19] X. Buffat, W. Herr, N. Mounet, T. Pieloni, and S. White, "Stability diagrams of colliding beams in the large hadron collider," *Phys. Rev. ST Accel. Beams*, vol. 17, p. 111002, Nov 2014.

[20] H. Grote, F. Schmidt, and L. H. A. Leunissen, "LHC Dynamic Aperture at Collision," Tech. Rep. LHC-PROJECT-NOTE-197, CERN, Geneva, Aug 1999.

[21] Y. Luo and F. Schmidt, "Dynamic Aperture Studies for LHC Optics Version 6.2 at Collision," Tech. Rep. LHC-PROJECT-NOTE-310, CERN, Geneva, Jan 2003.

[22] M.Crouch *et al.*, "Dynamic aperture studies of long-range beam-beam interactions at the LHC," in *Proceedings, 8th International Particle Accelerator Conference (IPAC 2017): Copenhagen, Denmark*, p. THPAB056, 2017.

[23] J. B. García *et al.*, "Beam-beam studies for FCC-hh," in *Proceedings, 8th International Particle Accelerator Conference (IPAC 2017): Copenhagen, Denmark*, p. TUPVA026, 2017.

[24] J. B. García *et al.* EuroCirCol Meeting Oct 2017, Presentation at the LHC machine committee, October, 2017.

[25] C. Tambasco, S. Arsenyev, J. Barranco García, X. Buffat, T. Pieloni, L. Rivkin, and D. Schulte, "Landau damping studies for the fcc: Octupole magnets, electron lens and beam-beam effects," in *9th Int. Particle Accelerator Conf.(IPAC'18), Vancouver, BC, Canada, April 29-May 4, 2018*, p. thpaf074, JACOW Publishing, Geneva, Switzerland, 2018.

[26] T. Pieloni *et al.*, "Colliding High Brightness Beams in the LHC," in *Proceedings, HB2012, Beijing, China*, p. MOP250, 2012.

[27] X. Buffat, N. Biancacci, S. V. Furuseth, D. Jacquet, E. Metral, D. Pellegrini, M. Pojer, G. Trad, D. Valuch, J. Barranco Garcia, T. Pieloni, C. Tambasco, and Q. Li, "Probing the behaviour of high brightness bunches in collision at 6.5 TeV and the interplay with an external source of noise (MD1433)," Apr 2017.

[28] S. V. Furuseth and X. Buffat, "Modeling of nonlinear effects due to head-on beam-beam interactions," *Phys. Rev. Accel. Beams*, vol. 21, p. 081002, Aug 2018.

[29] M. Giovannozzi, R. De Maria, and S. Fartoukh, "Specification of a System of Correctors for the Triplets and Separation Dipoles of the LHC Upgrade," in *Proceedings, 4th International Particle Accelerator Conference (IPAC 2013): Shanghai, China, May 12-17, 2013*, p. WEPEA048, 2013.

[30] G. Sabbi and E. Todesco, "Requirements for nb3sn inner triplet and comparison with present state of the art," in *HILUMILHC-MIL-MS-33*, 2012.

[31] E. Todesco, B. Bellesia, J.-P. Koutchouk, and C. Santoni, "Estimating field quality in low-beta superconducting quadrupoles and its impact on beam stability," in *LHC-PROJECT-Report-1061*, 2017.

[32] A. Ferrari, P. Sala, A. Fasso, and J. Ranf, "FLUKA: a multi-particle transport code," Tech. Rep. CERN-2005-10, 2005.

[33] T. Böhlen, F. Cerutti, M. Chin, A. Fassò, A. Ferrari, P. Ortega, A. Mairani, P. Sala, G. Smirnov, and V. Vlachoudis, "The FLUKA code: Developments and challenges for high energy and medical applications," *Nuclear Data Sheets*, vol. 120, pp. 211–214, 2014.

[34] G. Apollinari, I. B. Alonso, O. Bruning, P. Fessia, M. Lamont, L. Rossi, and L. Tavian, "High-luminosity large hadron collider (HL-LHC) technical design report v.0.1," Tech. Rep. CERN-2017-007-M, 2017.

[35] E. Skordis, R. Bruce, F. Cerutti, A. Ferrari, P. Ortega, P. Hermes, A. Lechner, A. Mereghetti, S. Redaelli, and V. Vlachoudis, "Impact of beam losses in the LHC collimation regions," in *Proc. 6th International Particle Accelerator Conference (IPAC'15)*. CERN-ACC-2015-271.

[36] F. Cerutti *et al.*, "Beam loss studies in IP." talk, FCC week 2018, Amsterdam, Netherlands, April 2018, 2018.

[37] A. Infantino, B. Humann, and F. Cerutti, "Energy deposition from collision debris in FCC-hh EIR," 2018.

[38] D. Schoerling, "Review of peak power limits for high-luminosity IR triplet magnets," 2017.

[39] L. Bottura, "11T magnet operating margin," 2018.

[40] R. Walker, "Synchrotron radiation," in *CAS – CERN Accelerator School : 5th General Accelerator Physics Course*, vol. 1, pp. 437–454, Geneva, Switzerland: CERN, 1992. doi: 10.5170/CERN-1994-001.437.

[41] M. Boscolo and H. Burkhardt, "Tools for flexible optimisation of IR designs with application to FCC.," in *Proc. 6th International Particle Accelerator Conference IPAC15*, pp. 2072–2074 TUPTY031, 2015.

[42] L. Deniau, H. Grote, G. Roy, and F. Schmidt, *The MAD-X program: Methodical Accelerator Design User's Reference Manual.* CERN, Geneva, Switzerland, 10 2018. http://cern.ch/madx/.

[43] A. Naumann, B. Bellenot, D. Piparo, E. Tejedor, G. Amadio, L. Moneta, O. Couet, P. Canal, and V. Vassilev, *ROOT: Data Analysis Framework User's Guide.* CERN, Geneva, Switzerland, 5 2018. https://root.cern.ch/.

[44] S. A. et al., "Geant4a simulation toolkit," *Nuclear Instruments and Methods in Physics Research Section A: Accelerators, Spectrometers, Detectors and Associated Equipment*, vol. 506, no. 3, pp. 250 – 303, 2003.

[45] F. Collamati, M. Boscolo, H. Burkhardt, and R. Kersevan, "Synchrotron radiation backgrounds for the fcc-hh experiments," *Journal of Physics: Conference Series*, vol. 874, no. 1, p. 012004, 2017.

[46] R. Kersevan, M. Ady, and J. Pons, *Molflow–SynRad: A Monte Carlo Simulator package developed at CERN.* CERN, Geneva, Switzerland. https://molflow.web.cern.ch/.

[47] J. Abelleira, L. Van-Riesen Haupt, *et al.*, "An alternative final-focus system for the fcc-hh: triplet optimization with energy deposition studies," *submitted for publication*, 2018.

[48] L. van Riesen-Haupt, J. Abelleira, E. C. Alaniz, and A. Seryi, "A Code for Optimising Triplet Layout," in *Proc. of International Particle Accelerator Conference (IPAC'17), Copenhagen, Denmark, 14–19 May, 2017*, no. 8 in International Particle Accelerator Conference, (Geneva, Switzerland), pp. 2163–2166, JACoW, May 2017. https://doi.org/10.18429/JACoW-IPAC2017-TUPVA043.

[49] J. Abelleira, E. C. Alaniz, A. Seryi, and L. van Riesen-Haupt, "Energy Deposition Studies and Luminosity Evolution for the Alternative FCC-hh Triplet," in *Proc. 9th International Particle Accelerator Conference (IPAC'18), Vancouver, BC, Canada, April 29-May 4, 2018*, no. 9 in International Particle Accelerator Conference, (Geneva, Switzerland), pp. 352–355, JACoW Publishing, June 2018. https://doi.org/10.18429/JACoW-IPAC2018-MOPMK003.

[50] L. van Riesen-Haupt, J. Abelleira, E. C. Alaniz, and A. Seryi, "An Optimised Triplet for the Final Focus of the FCC-HH with a 40m Final Drift," in *Proc. 9th International Particle Accelerator Conference (IPAC'18), Vancouver, BC, Canada, April 29-May 4, 2018*, no. 9 in International Particle Accelerator Conference, (Geneva, Switzerland), pp. 364–367, JACoW Publishing, June 2018. https://doi.org/10.18429/JACoW-IPAC2018-MOPMK007.

[51] T. Pieloni *et al.*, "Beam-beam effects." FCC week 2018, Amsterdam, Netherlands, April 2018, 2018.

[52] A. Chancé *et al.*, "Status of the Beam Optics of the Future Hadron-Hadron Collider FCC-hh," in *Proc. of International Particle Accelerator Conference (IPAC'16), Busan, Korea, May 8-13, 2016*, no. 7 in International Particle Accelerator Conference, (Geneva, Switzerland), pp. 1470–1472, JACoW, June 2016. doi:10.18429/JACoW-IPAC2016-TUPMW020.

[53] A. Fedynitch, *Cascade Equations and Hadronic Interactions at Very High Energies*. PhD thesis, KIT, 2015. CERN-THESIS-2015-371.

[54] P. K. Skowronski *et al.*, "Advances in MAD-X using PTC," Tech. Rep. LHC-Project-Report-1016, 2007.

[55] S. Tygier, R. B. Appleby, H. Rafique, R. J. Barlow, and J. G. Molsen, "Recent development and results with the MERLIN tracking code," in *Proceedings, 8th International Particle Accelerator Conference (IPAC 2017): Copenhagen, Denmark*, p. MOPAB013, May, 2017.

[56] E. Todesco. Private Communication, 2017.

[57] R. K. Adair and H. Kasha, "The range of muons in rocks," in *Proceedings, 13th International Conference on Cosmic Rays, Denver, Colorado*, 1973.

[58] Particle Data Group. Passage of particles through matter, `http://durpdg.dur.ac.uk/lbl/index.html`, 2005.

[59] M. I. Besana, "Evaluation of the radiation field in the future circular collider detector," *Phys. Rev. Accel. Beams*, vol. 19, p. 111004, 2016.

[60] H. Rafique, A. Krainer, R. Appleby, and J. L. Abelleira, "Proton cross-talk and losses in the dispersion suppressor regions at the FCC-hh," in *Proceedings, 8th International Particle Accelerator Conference (IPAC 2017): Copenhagen, Denmark*, p. TUPIK037, May, 2017.

[61] J. L. Abelleira, H. Rafique, R. B. Appleby, M. I. Besana, and A. Seryi, "Cross-talk studies between FCC-hh experimental interaction regions," in *Proceedings, 8th International Particle Accelerator Conference (IPAC 2017): Copenhagen, Denmark*, p. TUPVA036, May, 2017.

[62] A. M. Louzguiti. Private Communication, 2018.

[63] H. M. Durand *et al.*, "HL-LHC Alignment Requirements and Associated Solutions," in *Proc. of International Particle Accelerator Conference (IPAC'17), Copenhagen, Denmark, 1419 May, 2017*, no. 8 in International Particle Accelerator Conference, (Geneva, Switzerland), pp. 1893–1896, JACoW, May 2017. https://doi.org/10.18429/JACoW-IPAC2017-TUPIK085.